

Secondary Ice Production - No Evidence of Efficient Rime-Splintering Mechanism

Johanna S. Seidel ^{1,2}, Alexei A. Kiselev ², Alice Keinert ², Frank Stratmann ¹, Thomas Leisner ¹, and Susan Hartmann ¹

¹Leibniz Institute for Tropospheric Research, Department of Atmospheric Microphysics, Leipzig, Germany

²Karlsruhe Institute of Technology, Institute of Meteorology and Climate Research, Atmospheric Aerosol Research Department, Karlsruhe, Germany

Correspondence: susan.hartmann@tropos.de

Abstract.

Mixed-phase clouds are essential for Earth's weather and climate system. Ice multiplication via secondary ice production (SIP) is thought to be responsible for the observed strong increase of ice particle number concentration in mixed-phase clouds. In this study, we focus on the rime-splintering also known as the Hallett-Mossop (HM) process, which still lacks physical and quantitative understanding. We report on an experimental study of rime-splintering conducted in a newly developed setup under conditions representing convective mixed-phase clouds in the temperature range of -4 °C to -10 °C. The riming process was observed with high-speed video microscopy and infrared thermography, while potential secondary ice particles (SI) in the super-micron size range were detected by a custom-build ice counter. Contrary to earlier HM experiments, where up to several hundreds of SI particles per mg rime were found at -5 °C, we found no evidence of productive SIP, which fundamentally questions the importance of rime-splintering. Further, we could exclude two potential mechanisms suggested as explanation for rime-splintering: freezing of droplets upon glancing contact with the rimer and fragmentation of spherically freezing droplets on the rimer surface. The break-off of sublimating fragile rime spires was observed to produce very few SI particles, insufficient to explain the large numbers of ice particles reported in earlier studies. In the transition regime between wet and dry growth, in analogy to phenomena of deformation of drizzle droplets upon freezing, we also observed formation of spikes on the rimer surface, which might be a source of SIP.

1 Introduction

Ice formation in mixed-phase clouds affects cloud radiative properties, impacts cloud electricity, precipitation formation and cloud lifetime and is therefore essential for Earth’s weather and climate systems. Primary ice particles are formed by ice nucleating particles (INPs) catalyzing the nucleation process or via homogeneous freezing at temperatures below around $-38\text{ }^{\circ}\text{C}$.

20 In situ and remote sensing measurements of ice crystal number concentration (ICNC) in mixed-phase clouds occasionally demonstrate a strong discrepancy between the ICNC and INP concentrations of one to four orders of magnitude at moderate supercooling (Hobbs, 1969; Hobbs and Rangno, 1985; Mossop, 1985b; Hobbs and Rangno, 1990; Hogan et al., 2002; Crosier et al., 2011; Crawford et al., 2012; Heymsfield and Willis, 2014; Lawson et al., 2015; Taylor et al., 2016; Lasher-Trapp et al., 2016; Huang et al., 2017; Ladino et al., 2017; O’Shea et al., 2017; Korolev et al., 2020; Luke et al., 2021; Ramelli et al., 25 2021; Li et al., 2021). Such discrepancy could be explained by secondary ice production (SIP) processes increasing the total ice particle number concentration by multiplication of pre-existing ice particles (Field et al., 2017; Korolev and Leisner, 2020; Chisnell and Latham, 1976; Connolly et al., 2006; Sun et al., 2010; Crawford et al., 2012; Yano et al., 2016; Sullivan et al., 2018; Sotiropoulou et al., 2020; Georgakaki et al., 2022). Newest studies suggest that SIP is the dominant ice formation process in mixed-phase clouds (Zhao and Liu, 2021; Zhao et al., 2023). According to Korolev and Leisner (2020), SIP might 30 proceed according to the following mechanisms: (a) droplet fragmentation during freezing (Takahashi and Yamashita, 1977; Wildeman et al., 2017; Lauber et al., 2018; Keinert et al., 2020; Kleinheins et al., 2021), (b) rime-splintering, (c) fragmentation during ice-ice particle collisions (Vardiman, 1978; Takahashi et al., 1995; Grzegorzczuk et al., 2023), ice fragmentation due to (d) thermal shock (Dye and Hobbs, 1968; King and Fletcher, 1976b), (e) sublimation (Oraltay and Hallett, 1989; Dong et al., 1994; Bacon et al., 1998) and (f) activation of INPs in transient supersaturation (e.g., Prabhakaran et al., 2020). Yet another SIP 35 mechanism occurring during the break-up of freezing droplets on impact with smaller ice particles, suggested by Phillips et al. (2018), was supported experimentally by James et al. (2021). None of these proposed SIP mechanisms has been sufficiently characterized so far.

The most widely accepted SIP mechanism is the Hallett-Mossop or more generally rime-splintering process (Hallett and Mossop, 1974; Mossop and Hallett, 1974), which suggests that the secondary ice (SI) particles are produced upon riming 40 of a large ice particle (called rimer). Riming results from droplet–ice collisions as the ice particle falls through a cloud of supercooled droplets. Rime-splintering was identified in laboratory experiments to be active in a narrow air temperature range between $-3\text{ }^{\circ}\text{C}$ and $-8\text{ }^{\circ}\text{C}$ (Hallett and Mossop, 1974). They found a maximum SIP rate of around 350 SI particles per mg of accreted rime at near $-5\text{ }^{\circ}\text{C}$ and at a rimer velocity of 2.7 m s^{-1} . Similar results were obtained by Mossop in the follow-up experiments (Mossop, 1976, 1985a). Therefore, the temperature range from $-3\text{ }^{\circ}\text{C}$ to $-8\text{ }^{\circ}\text{C}$ is often referred to 45 as the ‘Hallett-Mossop temperature regime’. Heymsfield and Mossop (1984) highlighted the importance of the rimer surface temperature, which can be higher than the air temperature due to the latent heat of crystallization released upon freezing of accreted droplets (Heymsfield and Mossop, 1984). Generally, the freezing of a supercooled water droplet can be subdivided into three stages (Macklin and Payne, 1967). In the initial freezing or recalescence stage, ice dendrites rapidly grow through the droplet starting from the nucleation site, and the latent heat released during the phase transition causes the temperature

50 of the droplet to rise to the melting point of water ($0\text{ }^{\circ}\text{C}$) (Macklin and Payne, 1967; Pruppacher and Klett, 2010; Korolev and Leisner, 2020). In the subsequent second freezing stage, where the remaining liquid water freezes, the droplet temperature stays at $0\text{ }^{\circ}\text{C}$ as heat dissipation to the environment via heat conduction balances the latent heat of crystallization. After freezing is completed, the droplet cools down to the temperature of the environment. Freezing of a small droplet upon collision with a larger ice particle follows the same pathway but with a higher rate (100x) of latent heat removal through the water–ice boundary, 55 so that the temperature of the droplet may not reach the melting point at all. However, if the droplet mass accretion rate is high, the rimer surface temperature could rise to the melting point of water, signifying the transition from dry to wet growth regime (Schumann–Ludlam limit, Schumann, 1938; Ludlam, 1958; Pruppacher and Klett, 2010). The wet growth regime is thought to inhibit rime-splintering (Bader et al., 1974; Pruppacher and Klett, 2010; Korolev and Leisner, 2020, and references therein). Following the initial experiments by Hallett and Mossop, a connection between the droplet size distribution (DSD) 60 and the rate of SIP due to rime-splintering has been identified in the later experimental studies. In particular, the efficiency of rime-splintering was found to be the highest if droplets smaller than $12\text{ }\mu\text{m}$ and larger than $24\text{ }\mu\text{m}$ in diameter were present at the same time (Hallett and Mossop, 1974; Mossop, 1978a, 1985a). The rimer velocity also seems to be a relevant parameter for rime-splintering with reported maximum SIP rates observed between 2 m s^{-1} and 6 m s^{-1} (Mossop, 1976, 1985a; Saunders and Hosseini, 2001). Despite multiple evidence of the rime-splintering SIP from laboratory experiments and in situ observations, 65 the mechanism responsible for the release of SI splinters is still debated. Several mechanisms have been proposed that might cause SIP during riming based on the release of stresses due to mechanical action (shedding), pressure or thermal gradients during riming, freezing initiation of a droplet that makes glancing contact with the rimer or detachment of frail ice needles by sublimation (Mossop, 1976; Choulaton et al., 1980; Dong and Hallett, 1989).

Two types of experimental methods have been applied to study rime-splintering in laboratory, either using a single fixed 70 ice grain simulating realistic graupel (Brownscombe and Hallett, 1967; Aufdermaur and Johnson, 1972; Bader et al., 1974) or mimicking falling rimers by large, rotating ice-covered metal rods in a cloud simulation chamber filled with supercooled droplets produced by steam from a boiler (Hallett and Mossop, 1974; Mossop, 1976, 1985a; Saunders and Hosseini, 2001). In the following discussion, we refer to HM-type experiments corresponding to the latter case. For all of these experimental methods, the conditions regarding temperature, DSD and impact velocity were mostly comparable to those encountered in 75 the atmosphere. However, the information about droplet-rimer collision rates and rimer surface temperature is often missing. Simultaneous microscopic observation of the riming surface in an air flow and detection of SI particles have not been performed to date. In many cases, the existence of background ice particles in the simulation chamber led to large uncertainties in determined SIP rates. Difficulties in controlling the experimental conditions have apparently been responsible for the low replicability of the measured SIP rates that have been reported to be in the range from 0 to 8000 SI particles per mg rime at 80 similar conditions (Korolev and Leisner, 2020). It is remarkable that a significant number of SI particles is reported mainly from the HM-type experiments using large rimer surfaces and steam generation of cloud droplets, with the exception of the study from Latham and Mason (1961). In the latter study, however, the presence of carbon dioxide probably caused the high number of splinters (Korolev and Leisner, 2020).

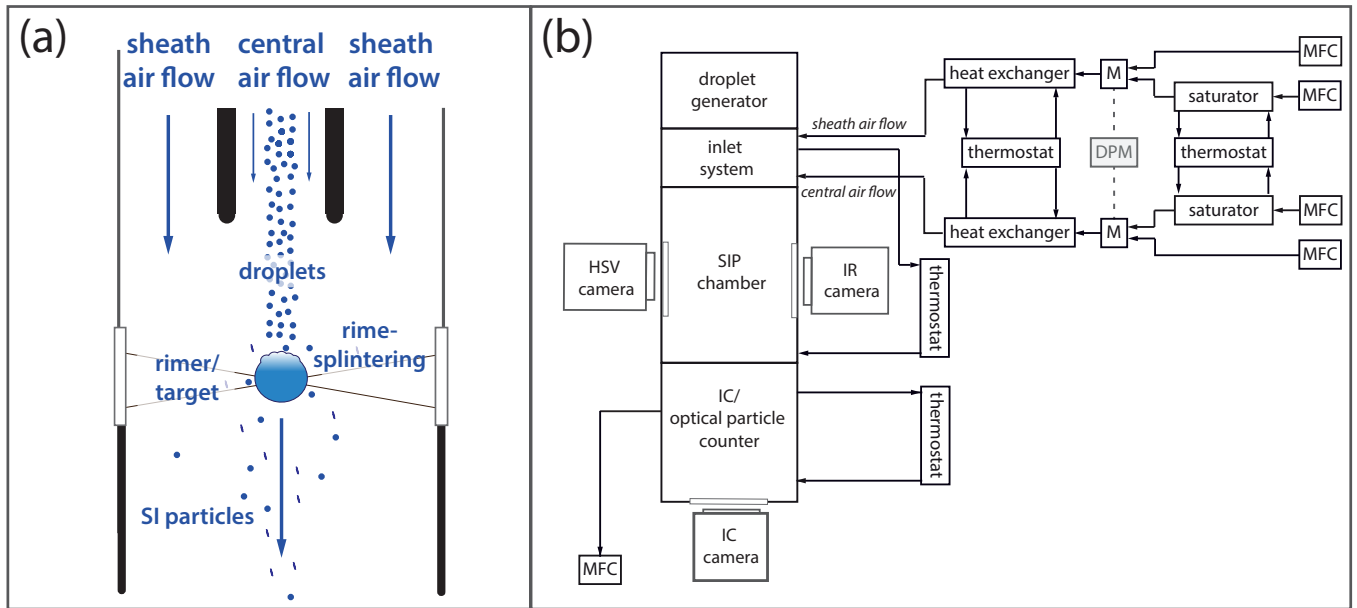


Figure 1. Sketches of (a) SIP chamber; (b) schematic of IDEFIX with flow conditioning system, droplet generator, inlet system, SIP chamber with high speed video (HSV) camera, infrared (IR) thermography system and Ice Counter (IC).

The overview of the previous experimental results indicates the necessity to revisit the rime-splintering experiments under better controlled conditions and with improved measuring techniques. For this purpose, the new laboratory experiment IDEFIX (Ice Droplets splintEring on FreezIng eXperiment) was set up, allowing direct observation of the riming process on the surface of a fixed graupel particle with high-speed video microscopy and infrared thermography, while detecting the SI particles with a newly developed ice counter.

2 Ice Droplets splintEring on FreezIng eXperiment (IDEFIX)

The experimental setup IDEFIX has been developed to study SIP resulting from riming on a qualitative and quantitative level for atmospheric representative and well-controlled conditions. In IDEFIX, riming is simulated by exposing a fixed large ice particle (diameter ≈ 1 mm) to a stream of supercooled water droplets carried by an air flow. The rimer was produced by freezing a drop of $1 \mu\text{L}$ deionized water placed at the intersection of two carbon fibers with a thickness of about $6 \mu\text{m}$ (Fig. 1a). The air flow velocity corresponds to the terminal fall velocity of a graupel grain of 1 mm in diameter, which is approximately 1 m s^{-1} . IDEFIX provides thermodynamic and flow conditions and allows for visualization of the riming process, measurement of the graupel surface temperature, and quantification of the production rate of the SI particles.

2.1 Experimental setup

IDEFIX consists of a pre-conditioning system, a droplet generator, an inlet system, the SIP chamber, and the SI particle detection system (Fig. 1b). IDEFIX is fed with two air flows, i.e., the central and the sheath air flows, each independently conditioned with respect to temperature, humidity and flow rate. Thereto, particle-free dry and humidified air (Nafion saturator, Gasmot) are mixed in turbulent mixing chambers (M) and subsequently cooled to the required temperature inside the heat exchangers controlled by a thermostat (FP50, Julabo). In the experiments described here, the central and the sheath air flows have the same temperature.

The central and the sheath air flows are isokinetically combined in an inlet system upstream of the SIP chamber. Flow conditions inside the SIP chamber are laminar. For a subset of experiments simulating higher droplet impact velocities, the central air flow was increased by up to factor of three. The supercooled droplets, generated by a droplet generator, are injected into the central air flow in the inlet system. Upon entering the SIP chamber, the droplets are supercooled for approx. 5 s and in thermal equilibrium with the air flow, as the thermal relaxation time of 20 μm droplets is on the order of 20 ms. The temperature of the inlet and the metal walls of the SIP chamber are controlled by a thermostat (F25, Julabo). The inner diameter of the SIP chamber (17 mm) was chosen to minimize the potential losses of SI particles to the walls by impaction of splintered SI particles. As worst case scenario we consider a 20 μm diameter particle ejected from the rimer surface with 10 m s^{-1} . In this case the stopping distance is about 7 mm. Downstream the SIP chamber either an optical particle counter WELAS[®] (WELAS[®] 1000, PALAS[®]), or the newly developed ice particle counter, is installed to determine the DSD, or the total number of SI particles, respectively.

In this study, the air flow temperature was varied in the range between -4°C and -10°C and the air flow velocity between 1 m s^{-1} and 3 m s^{-1} . Due to the systematic temperature deviation at the rimer position of around +1 K, the water vapor saturation with respect to ice is 90%. Water vapor emitted by evaporating water droplets contributes less than 1% RH and can be neglected.

2.2 Droplet generation and size distributions

A monodisperse droplet generator (MDG, model 1530, TSI[®]) is used for generating droplets with different size distributions. In the MDG, mechanical vibration of the nozzle combined with aerodynamic focusing produces a jet of deionized water droplets (details are described in Duan et al., 2016). The DSD and total droplet number can be controlled by adjusting the liquid flow rate, vibration frequency, and the focusing air flow rate. To study the impact of different droplet sizes on the efficiency of rime-splintering SIP, four different MDG settings were used and the resulting DSDs were measured with an optical particle counter WELAS[®]. The MDG settings and parameters of the log-normal fits of the DSDs are given in Table 1 and shown in Fig. 2.

As the droplets produced by the MDG are intrinsically charged, two bipolar corona discharges operating at 50 Hz alternating voltage of 5 kV were used to partly neutralize the droplets prior to entering the inlet system. This has significantly improved the stability of droplet generation.

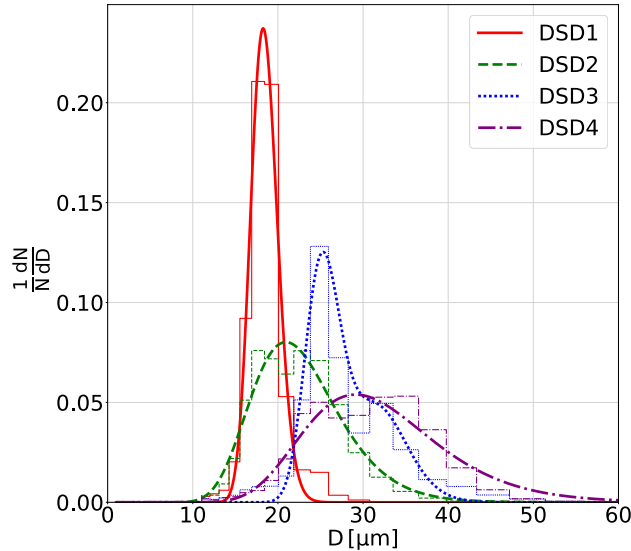


Figure 2. Normalized number size distributions of four different droplet populations used in the IDEFIX experiments (DSD1–DSD4) including measurements (bar graph) and respective log-normal fits (curves, parameters are given in Table 1).

Table 1. MDG settings frequency F , liquid flow rate Q and flow focusing pressure difference ff resulting in four different droplet size distributions DSD1–4, which were found to be log-normally distributed applying $\frac{1}{N} \frac{dN}{dD} = \frac{1}{\sqrt{2\pi \ln \sigma_g}} \exp\left(-\frac{(\ln D - \ln D_g)^2}{2 \ln \sigma_g^2}\right)$. Given are the geometric mean diameter D_g and geometric standard deviation factor σ_g of the log-normal distributions fitted to DSD1–4 (Fig. 2). For DSD3 a bimodal fit was applied and the relative fraction of mode1 and 2 is 0.7 and 0.2, respectively. The goodness of fit is described by the coefficient of determination R^2 .

DSD	MDG settings			Fit parameter		
	F [kHz]	Q [mL h ⁻¹]	ff [psi]	D_g [μm]	σ_g	R^2
DSD1	220	2	2.6–2.8	18.4	1.1	0.99
DSD2	off	2	2.6–2.8	22.1	1.3	0.97
DSD3	100	2	1.4–1.6			
mode1				25.3	1.1	0.97
mode2				32.1	1.1	0.97
DSD4	off	2	1.4–1.6	31.0	1.3	0.94

130 2.3 Riming observation

For microscopic and thermal observation of the riming process a high speed video (HSV) camera (Phantom Veo 710L, HSVision) and an infrared camera (IR, ImageIR 7340, InfraTec GmbH) were used. The HSV camera was operated with a 10x microscopic objective (Plan Apo, Mitutoyo) in the transmitted illumination. This setup allowed for an exposure time of 2 μs ,

a focal depth of about 200 μm and a pixel resolution of about 2 μm . The field of view (FOV), as well as the recording time, varied according to the selected frame rate. For low frame rates in the range of 100–1000 fps the maximum frame size was 1280 x 800 Pixel corresponding to the FOV of 3.5 x 1.6 mm. With this setting, it was possible to observe the evolving rimer surface structure over a time period of several seconds. In order to record individual droplet–rimer collisions with high frame rates (up to 70000 fps), the maximum frame size was reduced to 256 x 256 Pixel (FOV 0.5 x 0.5 mm).

The IR camera was operated with a 2x germanium macroscopic lens and provided measurements of the rimer temperature with accuracy of ± 1 K, based on the factory calibration in the temperature range from -30 $^{\circ}\text{C}$ to 300 $^{\circ}\text{C}$, as described in Kleinheins et al. (2021). In the IR calibration experiment (Appendix C), the rimer surface of true temperature 0 $^{\circ}\text{C}$ was found to appear 1.4 ± 0.6 K colder in the IR measurements. This offset, which can be attributed to the presence of Ge-windows and proximity of chamber walls, should be kept in mind when considering the diagrams showing the IR temperature values. The IR video sequences have been recorded with a frame rate of 25 fps.

2.4 Ice particle detection

To count the SI particles, a custom-build Ice Counter (IC) is installed downstream of the SIP chamber of IDEFIX. The cross section of the IC is shown in Fig. 3a. SI particles and droplets carried by the air flow are directed onto the surface of a sucrose solution (MerckTM, 42.85 wt %) kept at a temperature just below its melting point. As the sucrose solution is slightly supercooled, impinging ice crystals grow slowly to optically detectable sizes whereas liquid droplets dissolve in the solution upon contact. The melting point for this sucrose concentration was determined experimentally to be -5.0 $^{\circ}\text{C}$ and the solution was kept at -5.7 $^{\circ}\text{C}$ throughout the experiments. The method of using a supercooled sugar solution for ice crystal detection was first introduced by Bigg (1957) and has been popular for detecting ice crystals in laboratory experiments (e.g. Mason and Maybank, 1960; Aufdermaur and Johnson, 1972; Kolomeychuk et al., 1975). By heating the sugar solution above the melting point, ice crystals melt and a new experimental cycle can be started without the need to exchange the sucrose solution. The sucrose bath is illuminated from above with two white LEDs and the ice crystals floating on the surface of the sucrose solution are observed with a video camera (Photonfocus MV1-D2080-160-G2) through the transparent windows of the cooling cell from below. An example of ice crystals grown in the IC bath is shown in Fig. 3b. The impaction probability of an ice crystal on the surface of the sucrose solution is higher for larger ice crystals and higher flow velocity. The flow in the IC is accelerated through a nozzle of 3.5 mm diameter at the end of the conical flow tube connected to the SIP chamber (see Fig. 3a). At this nozzle size and a total air flow rate of 12.35 L min^{-1} the impaction cut-off aerodynamic diameter of 2 μm has been found experimentally. However, taking into account that secondary ice crystals are exposed to subsaturated conditions with respect to ice and sublimate on their way to the IC, the 2 μm cut-off diameter at the collision point would correspond to an initial ice particle diameter of 3.3 μm released in the vicinity of the rimer. Details of the IC characterization experiments can be found in Sect. A1 in the Appendix. To ensure that there are no background counts, every experiment has been preceded and followed by a blank test, where a rimer was situated in the SIP chamber and exposed to a droplet-free air flow for at least about 2 min. Only the experiments where no ice appeared in the IC sucrose solution are considered as valid.

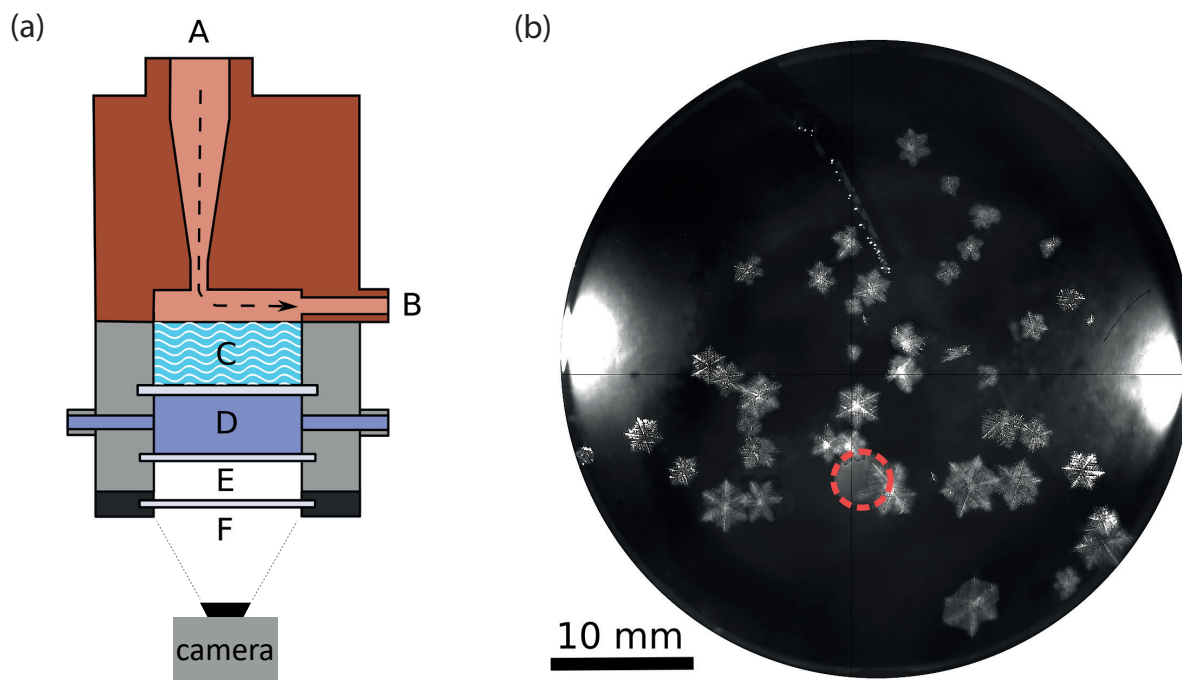


Figure 3. Ice Counter (IC) used to detect the SI particles via impaction on supercooled sucrose solution. In panel (a), a cross-section of the IC is shown including inlet (A), outlet (B), sucrose bath (C), flow-through chamber with cooling liquid (D), thermal isolation cell with two transparent windows (E) and camera setup (F). The entire IC housing is cooled by ethanol flowing through the chamber (D) and the copper housing body (not shown). In panel (b), an example of ice crystals in the supercooled sucrose solution is given. The bright spots on the left and right side are the LED lights installed in (C) for illumination. A PT-100 temperature sensor is immersed into the sucrose solution to measure its temperature. The nozzle position is marked by the dashed red circle.

3 Results and discussion

3.1 Riming

Growth Regimes

170 Riming experiments were conducted with four different droplet populations as described in the experimental section. For each DSD, the respective collision rates have been calculated as described in the Appendix (see Sect. B1+B2) and can be found in Table 2 together with the relevant experimental parameters. Depending on the settings (DSD1–4, see Fig. 2), three different riming regimes were observed at IDEFIX: dry (a), wet (b) and transition growth (c). Examples of the characteristic time series of the rimer surface temperature before, during and after riming are given in Fig 4.

175 Dry growth was observed for low mass collision rates associated with DSD1 and DSD2. In all experiments with these settings, the rimer surface temperature increased by a constant value of about 0.3 K to 2 K during riming, as shown in Fig. 4a.

Table 2. IDEFIX parameter space for SIP experiments.

Air flow temperature	$-4\text{ }^{\circ}\text{C}, -5\text{ }^{\circ}\text{C}, -7\text{ }^{\circ}\text{C}, -10\text{ }^{\circ}\text{C}$
Maximum air flow velocity	$1\text{ m s}^{-1}, 3\text{ m s}^{-1}$
Ice particle (rimer) diameter	$\approx 1\text{ mm}$
Range of droplet diameters	$10\text{--}50\text{ }\mu\text{m}$
Avg. number collision rate	$(3.6\text{--}8.7) \times 10^2\text{ mm}^{-2}\text{ s}^{-1}$
Avg. mass collision rate	$(1.6\text{--}16) \times 10^{-3}\text{ mg mm}^{-2}\text{ s}^{-1}$
Impaction cut-off diam. in IC	$2.0\text{ }\mu\text{m}$
Ice crystal detection limit	$3.3\text{ }\mu\text{m}$

After riming, the rimer surface temperature returns to the environment temperature. In the wet growth regime (Schumann, 1938) resulting from high mass collision rates, the latent heat released by freezing of continuously colliding droplets cannot be removed rapidly enough by heat dissipation and sublimation, so that the surface temperature of the rimer rises to the melting point of water (see heat balance model of a riming particle in Appendix Sect. B1) and a liquid layer forms at the graupel surface (Fig. 4b). In the cases where the collision rate varied with time, the rimer surface temperature was observed to oscillate between the melting point and a lower temperature. We describe this as transitional growth regime (see Fig. 4c). Wet growth as well as the transitional growth regime was occasionally observed with DSD3 and DSD4.

Microscopic structure of rime

In the dry growth regime, the structure of rime is independent of the collision rate, because the individual droplets colliding with the rimer freeze completely before the next droplet arrives. In the experiments described here, the inter-arrival time between two consecutive droplets hitting the same spot on the rimer surface was between 0.4 and 0.6 s, as calculated with Eq. D3 in Appendix Sect. D. This is significantly longer than the time of individual droplets freezing which was calculated to be between 0.01 s and 0.04 s, (Eq. D1, D2 in Sect. D) assuming droplets with semi-spherical cap geometry freezing on ice surface at a temperature between $-10\text{ }^{\circ}\text{C}$ to $-5\text{ }^{\circ}\text{C}$, respectively.

Upon collision with the rimer surface, a droplet starts spreading to assume the equilibrium shape determined by the surface energy relationship between ice, water, and gas phase. However, the spreading is counteracted by freezing, which is also initiated at the moment of contact. Contrary to the freezing rate, the spreading rate does not depend on the temperature in the range between $-3\text{ }^{\circ}\text{C}$ and $-8\text{ }^{\circ}\text{C}$; the final shape of an accreted droplet is therefore defined by the time required to halt the spreading. The HSV records taken at $-5\text{ }^{\circ}\text{C}$, $-7\text{ }^{\circ}\text{C}$ and $-10\text{ }^{\circ}\text{C}$ in Fig. 5 show different shapes of accreted droplets. At $-10\text{ }^{\circ}\text{C}$, the accreted frozen droplets retain their quasi-hemispherical shape with apparent contact angle between 80° and 120° . Multiple frozen droplets are forming narrow ice spicules at this temperature. At temperatures above $-10\text{ }^{\circ}\text{C}$, droplets spread to flat lentil shapes with apparent contact angles of about $30^{\circ} \pm 10^{\circ}$, forming thick rime columns.

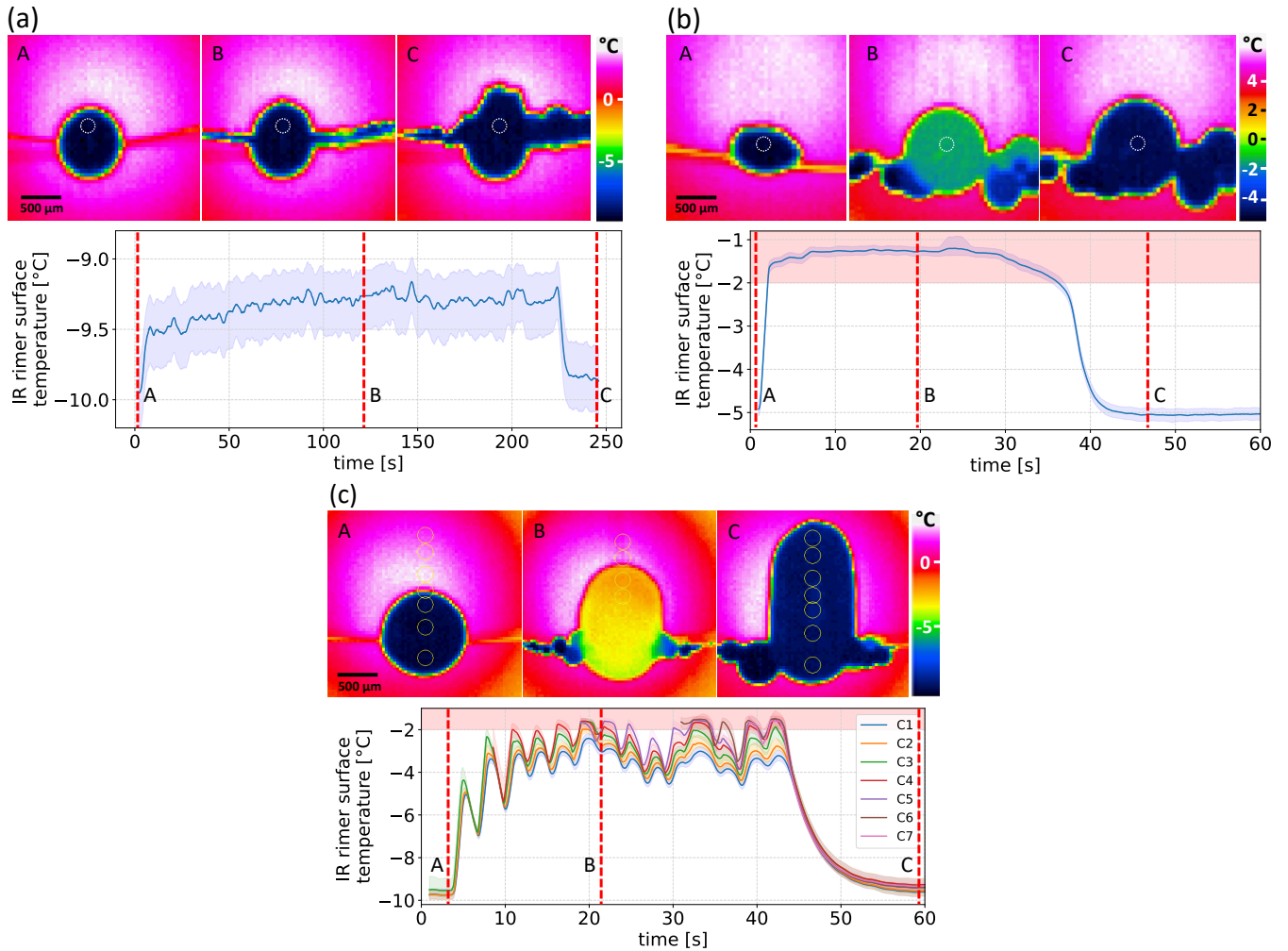


Figure 4. Sequence of IR images (A) before, (B) during and (C) after riming (upper panel) and time series of the average rimer surface temperature measured within circles of 150–200 μm diameter close to the rimer top in the IR images for dry (a), wet (b) and transitional growth regime (c). In example (c), several measurement circles (C1–C7, numbered from bottom to top) were applied. The red shaded areas mark the IR temperature region of the water melting point according to calibration measurements. Please note the different scales of the color bars.

The tendency to freeze in spherical shapes upon droplet accretion at lower temperatures was also observed by Macklin and Payne (1968, 1969) and Dong and Hallett (1989). The microscopic photographs of rime structures by Griggs and Choulaton (1986) also show preferential formation of fragile ice needles with decreasing temperature.

During riming in the transitional or wet growth regime, a dense ice particle with a smooth surface was formed at all investigated temperatures (Fig. 6, lower panel). In these growth regimes, the characteristic inter-arrival time is about 0.10 s and is

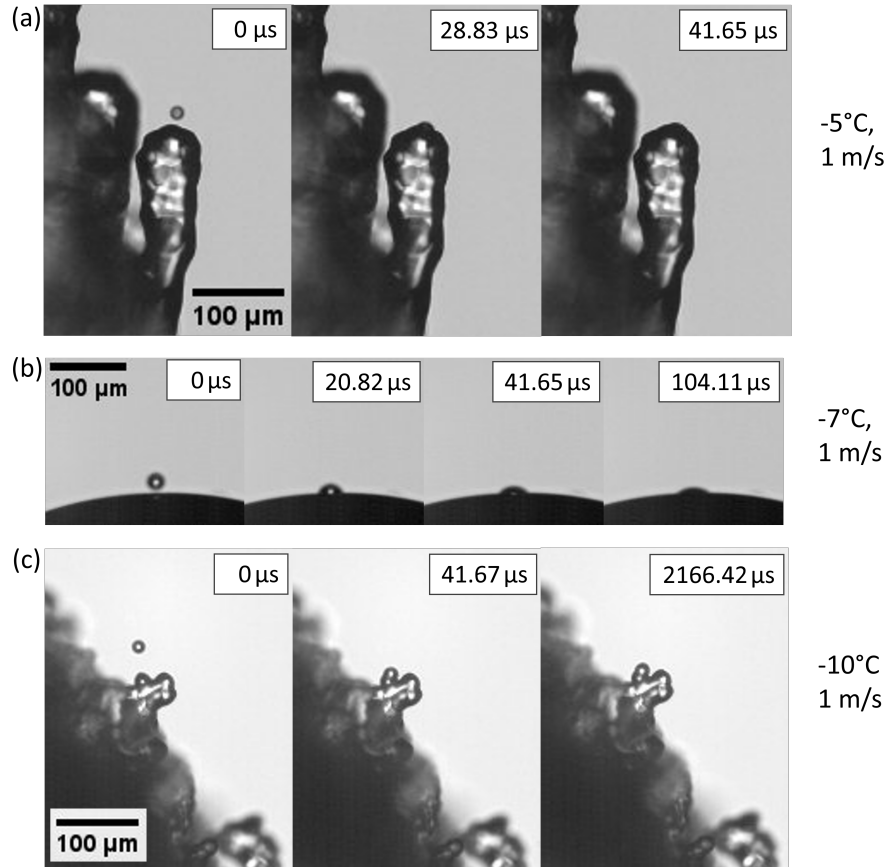


Figure 5. HSV-image sequence of individual droplet–rimer collisions with air flow velocity 1 m s^{-1} at -5°C and droplet diameter $D = 16.5 \mu\text{m}$ (a), -7°C and $D = 20 \mu\text{m}$ (b) and -10°C and $D = 18.5 \mu\text{m}$ (c) in the dry growth regime.

close to the freezing time of water droplets in the size range of $30\text{--}50 \mu\text{m}$ in diameter for the investigated temperature range in the IDEFIX experiments (approx. $0.08\text{--}0.23 \text{ s}$ at -5°C). Hence, larger accreted droplets are still partially liquid when the next droplets arrives at the same spot. This leads to continuous wetting of the rimer surface, thus impeding the growth of rime spires.

3.2 Rime-splintering

Out of 30 valid IDEFIX experiments with droplet–rimer mass collision rates in the range between $1.6 \times 10^{-3} \text{ mg mm}^{-2} \text{ s}^{-1}$ to $16 \times 10^{-3} \text{ mg mm}^{-2} \text{ s}^{-1}$, only in six experiments potential SIP events were identified by observing ice particles in the IC (cf. Table 3). A detailed overview of the valid rime-splintering experiments as well as HSV and IC images of the experiments with potential SIP are given in Table E1 and Fig. E1 in the Appendix. In two experiments at -5°C , ice particles were counted with the IC during riming, whereby no co-occurring SIP were seen in the high-speed video recordings. There were also four

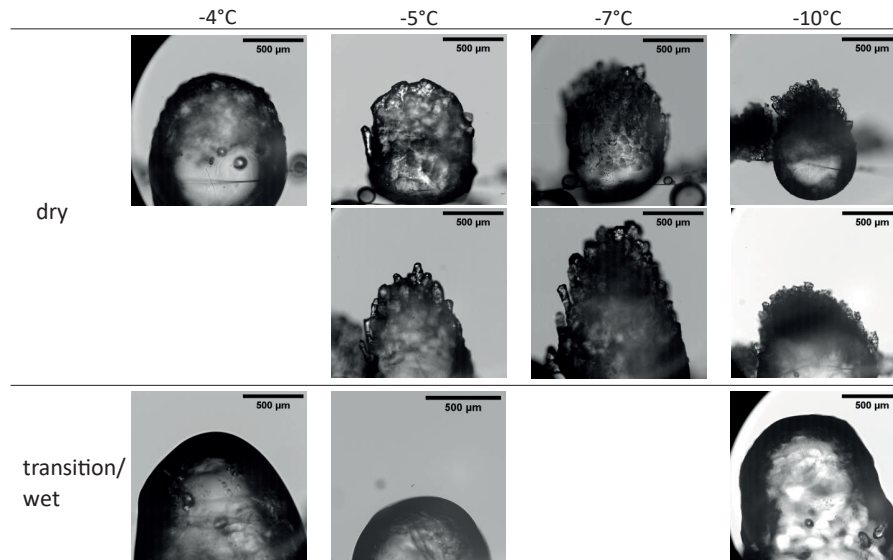


Figure 6. Macroscopic view on the graupel surface structure in a matured stage grouped by temperature and prevailing growth regime. In all cases the air flow velocity was set to 1 m s^{-1} .

Table 3. Number of valid IDEFIX experiments in total and where ice crystals were detected in the IC (potential SIP) during or after riming for all experimental temperatures. The number of cases in the different growth regimes is given in parentheses. In case of potential SIP, the number of detected ice crystals and the prevailing growth regime during the experiment is given as well. Further details can be found in Table E1.

	-4 °C	-5 °C	-7 °C	-10 °C
total	4	11	6	9
(dry/wet/transition)	(3/0/1)	(9/1/1)	(6/0/0)	(6/0/3)
during riming	0	2	0	0
observed number of ice crystals	20 (dry) 5 (dry/transition)			
after riming	0	0	1	3
observed number of ice crystals	1 (dry) 1 (dry) 2 (dry) 1 (transition)			

experiments at -7°C and -10°C , in which one or two individual ice crystals were detected in the IC several minutes after
 215 riming. Among these four cases, sublimation induced break-off of a rime spire was observed twice with the HSV camera. An

example of a rime-spire bending down before its final break-off, which was documented after about 10 min of sublimation, is shown in Fig. 7.

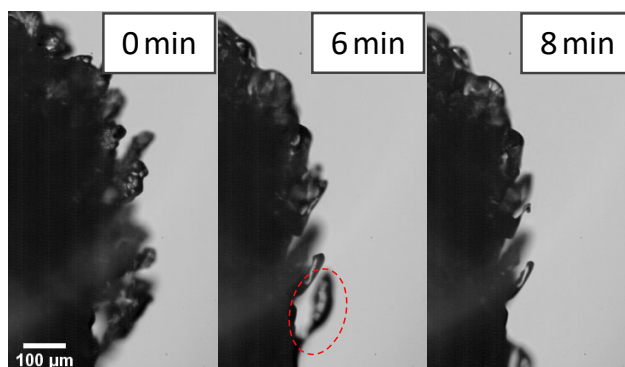


Figure 7. High speed image sequence of sublimating rime spires on the surface of a graupel particle at $-10\text{ }^{\circ}\text{C}$ in an ice subsaturated environment with air flow velocity 1 m s^{-1} after riming. After about 8 min of sublimation, the encircled rime-spire was observed to bend down, before it finally broke off two further minutes later.

The cases for which ice crystals were observed in the IC during riming could not be reproduced in other experiments conducted under the same conditions. We therefore conclude, that no efficient and reproducible SIP was observed during riming experiments with IDEFIX within the investigated parameter range (see Table 2). In all potential SIP cases, the number of ice crystals detected in the IC was well below the values expected on the basis of the original HM experiments (Hallett and Mossop, 1974; Mossop, 1976, 1985a) in the temperature range of $-3\text{ }^{\circ}\text{C}$ to $-8\text{ }^{\circ}\text{C}$. In their experiments, up to 300–350 SI particles per mg rime were observed at around $-5\text{ }^{\circ}\text{C}$ for rimer velocities in the range of $2\text{--}4\text{ m s}^{-1}$ and accretion rates on the order of $10^{-4}\text{ mg mm}^{-2}\text{ s}^{-1}$ (Mossop, 1985a). Summarizing all SIP experiments in the dry growth regime at $-5\text{ }^{\circ}\text{C}$, the number of detected ice crystals account for maximum 7.6 SI particles per mg. Note, that this derived SIP rate is determined by one out of five experiments (Table 3). We acknowledge the possibility that all SI crystals generated via rime-splintering were considerably smaller than $3.3\text{ }\mu\text{m}$ diameter and therefore could not be detected. The possible reasons for inefficient SIP in our experiments are summarized at the end of this section. In the following, we discuss the individual mechanisms potentially underlying the rime-splintering SIP (illustrated in Fig. 8) based upon our microscopic observation of riming events in more detail.

Splintering during freezing of an accreted droplet. This mechanism suggests that the SI particles are produced as a result of the fragmentation of ice shell forming around a freezing droplet (Mossop, 1976; Choulaton et al., 1980; Griggs and Choulaton, 1983) in analogy to shattering of droplets freezing in free fall (Kleinheins et al., 2021; Lauber et al., 2018; Keinert et al., 2020). As an ice shell forms around the freezing droplet, the pressure in the liquid water trapped inside increases considerably (up to 240 bar, Kleinheins et al., 2021). If pressure-induced stress exceeds tensile strength of ice, pressure is released by elastic deformation followed by fragmentation of the ice shell. An illustrative case of pressure induced fragmentation and splintering

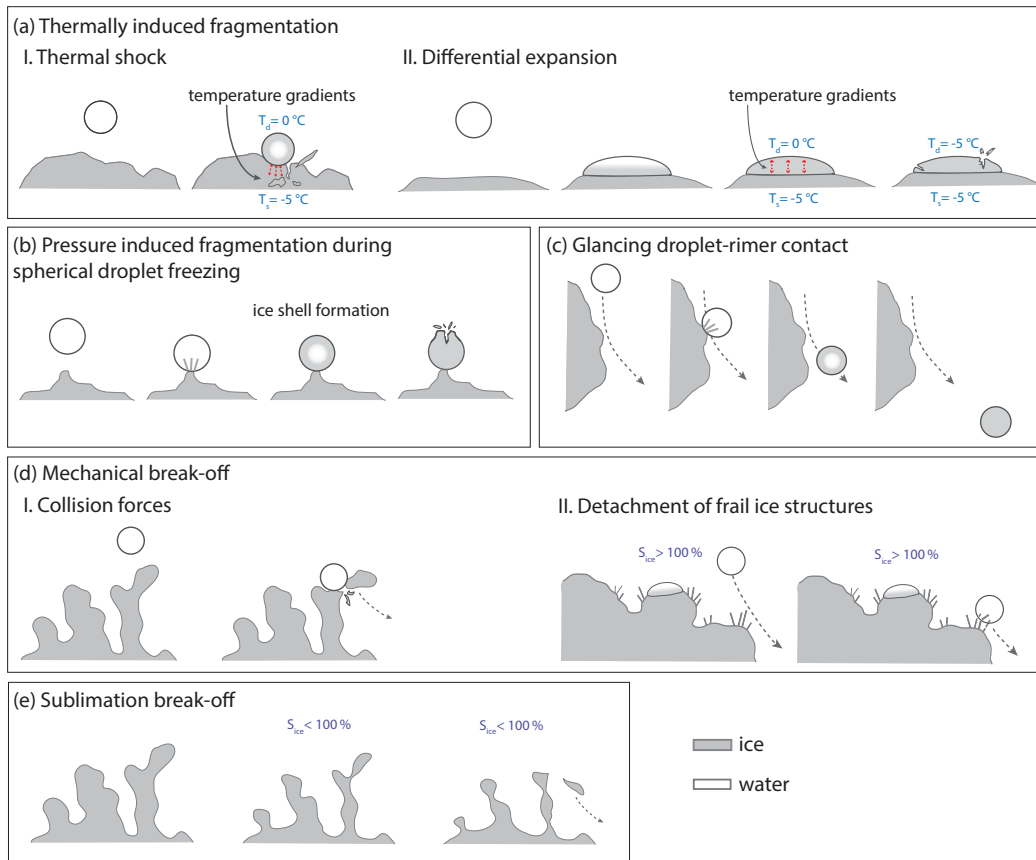


Figure 8. Schematic illustration of different mechanisms proposed to explain the rime-splintering SIP mechanism (a–d). A proposed mechanism, where riming leads indirectly to SIP is sketched in (e). In (a), temperature gradients are indicated with red arrows. The ice surface has an exemplary temperature of $T_s = -5^\circ\text{C}$ just like the incident supercooled droplet. During freezing upon impact, the droplet temperature (T_d) increases up to 0°C . Schematics (a-II) is adapted from the simplistic conceptual model and the observation of a shattered droplet from Dong and Hallett (1989, Fig. 12, 13). (b) is adopted from a camera observation of splintering due to ice shell fragmentation of a spherically shaped accreted presented in Choularton et al. (1980, Fig. 2c). In (d-II), saturation with respect to ice (S_{ice}) has to be over 100% to enable depositional growth of frail ice structures on the rimer surface. In an ice subsaturated environment (e), sublimation can lead to the fragmentation of rime spires previously grown on the graupel surface.

of a droplet accreted on a surface covered with ice at -7°C was observed by Choularton et al. (1980, Fig. 2c therein) and is shown schematically in Fig. 8b.

240 Formation of an ice shell enclosing a freezing droplet requires spherically symmetrical removal of latent heat of crystallization through the droplet surface, facilitated, e.g., by ventilation and droplet rotation in free fall. A stationary droplet accreted on the surface of a rimer could form an ice shell only if the heat flux through the contact surface is comparable with that of diffusion and convective heat removal through the air. This could be the case if the freezing droplet is connected to the rimer by

a thin neck, formed, for example, by a smaller frozen droplet present at the point of contact (Choularton et al., 1980; Emersic and Connolly, 2017).

245 Observations obtained with IDEFIX and reported in previous studies of Dong and Hallett (1989) and Emersic and Connolly (2017) have shown that the droplets tend to spread upon impact on smooth and rough ice surfaces at temperature above -10°C . This clearly contradicts the hypothesis of the pressure-induced fragmentation of the ice shell forming around the freezing droplet accreted to the rimer surface. Below -7°C , there is a distinct tendency of the accreted droplets to freeze in a spherical shape. However, in our experiments with IDEFIX, no SIP during riming was observed at -10°C . To this effect, 250 Griggs and Choularton (1983) speculated that at such low temperatures, the ice shell of an accreted freezing droplet might be too strong for cracking. This, contradicts the observation of Kleinheins et al. (2021) who reported pressure release events in freezing droplets down to the temperature of -25°C for much larger droplets.

Even if the ice shell is not forming around the freezing droplet, the latent heat released during freezing can induce thermal gradients at the droplet–ice interface and thus lead to differential thermal expansion of ice, which could result in fragmentation 255 of the freezing accreted droplet or the underlying ice structure, as illustrated in Fig. 8a-I and Fig. 8a-II, respectively. A detailed review of these thermal shock mechanisms is given in Korolev and Leisner (2020) and references therein.

Although the dry growth regime would have offered suitable conditions, no evidence was found for such SIP mechanisms associated with thermal shock (Koenig, 1963; King and Fletcher, 1976a) or shear stress release (Dong and Hallett, 1989) in IDEFIX experiments. Even if the large fraction of SI particles generated in this way would be smaller than $3.3\ \mu\text{m}$ in diameter 260 and have detection probabilities less than 50 % considering sublimation effects on the way to the IC, we expect that due to the high number of droplet collisions at IDEFIX (on the order of 2000 per experiment), at least a few SI particles would have been detected with the IC.

Droplet freezing induced by glancing contact with rimer surface, illustrated in Fig. 8c, can be considered as a SIP mechanism (Mossop, 1976). According to our statistical estimation, about 2 to 17 droplets per second are passing near the rimer 265 surface at a distance smaller than the median droplet diameter of $20\text{--}30\ \mu\text{m}$ (concept described in Wang, 2013). Based on this estimation, multiple frozen droplets should have been observed in the IC as their size would ensure their efficient impaction on the surface of the sucrose solution. As we do not observe continuous SIP, droplets experiencing a glancing contact with the rimer surface are always accreted by the surface or do not freeze upon glancing contact with ice. On a rare occasion when a droplet on a glancing trajectory was in the focal plane of the imaging optics, we have observed droplet coalescence with the 270 rimer surface (Fig. 9). The preferential accretion of grazing droplets is affirmed by the results of Emersic and Connolly (2017).

Another potential SIP associated with riming is *break-off of frail ice structures due to mechanical action or sublimation*. Fragile ice formations such as chains of frozen droplets or towers on the rimer surface (also called rime spires) or ice needles preferentially growing by vapor deposition on the rimer surface at around -5°C in an ice and water supersaturated environment (Libbrecht, 2017) are suggested to be a further potential source of SI particles associated with rime-splintering SIP (Macklin, 275 1960; Bader et al., 1974; Mossop, 1976). Those fragile ice structures may break off upon collisions with droplets or other ice particles (Mossop et al., 1974), as illustrated in Fig. 8d-I,II. Neither detachment of frail ice needles, nor mechanical break-off of rime spires was observed in IDEFIX in the investigated parameter space. Even at -10°C , the more fragile rime spires are

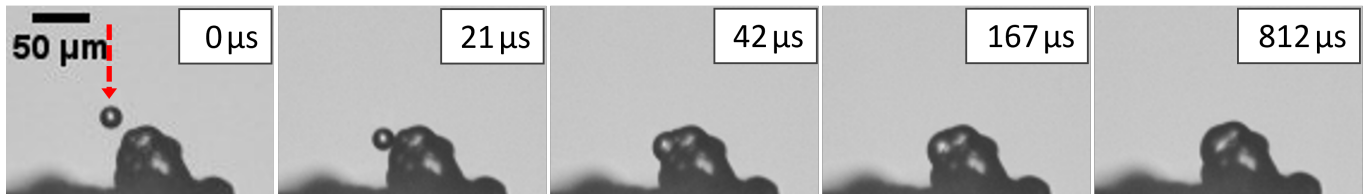


Figure 9. Glancing collision of a $20\ \mu\text{m}$ in diameter droplet resulting in accretion to the rimer surface at -7°C and $1\ \text{m s}^{-1}$. The arrow illustrates the trajectory of the droplet.

mechanically stable. Experiments by Griggs and Choulaton (1986) have shown that rime spires are unlikely to break off due to shear forces from air motion alone, and that relative velocities of above $60\ \text{m s}^{-1}$ are required for this to occur. Deposition
 280 growth of ice needles could not be observed at IDEFIX as the flow around the rimer is slightly subsaturated with respect to ice.

Sublimation break-off of rime spires can take place in ice subsaturated conditions and thus might be a mechanism for SIP (Mossop and Hallett, 1974; Oraltay and Hallett, 1989). Thereby, thinner parts of a rime spire or other fragile ice structure sublimate faster compared to thicker ice structures leading to ice particle separation and consequently to ice multiplication (Fig. 8e). Sublimational break-off was described for pristine ice crystals with aspect ratios larger than 3 favorable and rimed
 285 ice particles (Dong and Hallett, 1989; Dong et al., 1994; Bacon et al., 1998; Korolev and Leisner, 2020). **A very few cases of rime spire break-off due to sublimation were observed in IDEFIX after riming at -7°C and -10°C (cf. Table 3).**

Generally, fragmentation by sublimation can be thought as separate SIP process from rime-splintering (Korolev and Leisner, 2020), since riming plays only an indirect role leading to a finely structured graupel surface dominated by frail rime spires in the dry growth regime. Based on the argument of Korolev and Leisner (2020) and Korolev et al. (2020) that small ice fragments
 290 in a subsaturated cloud environment are more likely to fully sublimate before they return to a cloud zone supersaturated with respect to ice, it might be unlikely that this mechanism is important in atmospheric clouds. In contrast, Deshmukh et al. (2022) could theoretically derive a significant contribution of SIP due to sublimation taking also graupel into account. It is conceivable that the mechanism may be important in regions near the cloud edge where entrainment of dry air occurs, as discussed earlier by Bacon et al. (1998).

295

To discuss the possible reasons why no efficient SIP has been observed in the IDEFIX experiments in contrast to earlier HM-type experiments (Mossop et al., 1974; Mossop, 1976, 1978a, 1985a; Saunders and Hosseini, 2001), we compare the details of experimental set-ups. In the IDEFIX riming experiments, (i) the geometrical cross-sectional area of the rimer is about 1000 times smaller than in the HM-type setup, (ii) the droplet populations contained almost no droplets smaller than
 300 $12\ \mu\text{m}$ in diameter, (iii) the mass collision rates are a factor of 10 to 100 higher than in the original HM experiments, and (iv) the air flow in IDEFIX is not supersaturated with respect to ice. Nevertheless, the IDEFIX setup reproduces most of the processes that were previously thought to be responsible for SIP via riming splintering.

Whereas (i) in IDEFIX the rimer has a realistic graupel size of roughly 1 mm diameter, the rimer was unrealistically large in the previous HM-type experiments, where cylindrical metal rods (e.g. 30 cm x 0.24 cm) were used as rimer (Hallett and

305 Mossop, 1974; Mossop, 1976, 1985a; Saunders and Hosseini, 2001). Such a large riming surface would allow observation of effects that are statistically less frequent. In more detail the observation can be explained by either SIP as a continuous process producing low numbers of SI particles over the whole period of riming or a random burst event producing a high number of SI particles. In the second case, a rime-splintering event could be rare but produce a high number of SI particles, for example if a rimer has to undergo multiple sublimation-deposition growth cycles to develop frail dendrites that can easily break off.

310 To detect such events, significantly higher accretion rates, longer observation times, or a larger number of rimers need to be investigated. For the IDEFIX conditions, the accretion rate cannot be increased without undergoing dry-wet growth transition. Longer observation times at the IDEFIX riming rates or multiple rimers are not feasible with IDEFIX. Consequently, to be able to detect rare but efficient events a different experimental set-up would be required.

(ii) Only the IDEFIX setting with DSD2 contained droplets smaller than $12\ \mu\text{m}$. In that case, the concentration ratio of small

315 accreted droplets compared to droplets larger than $24\ \mu\text{m}$ was 0.05. This is lower than the concentration ratios from 0.1 to 2.0 (or higher) used in HM-experiments, in which the efficiency of rime-splintering was found to correlate with the accretion rate of droplets smaller than $12\ \mu\text{m}$ and larger than $24\ \mu\text{m}$ in diameter. Different droplet size distributions were tested in the HM-type experiments (e.g. Mossop and Hallett, 1974; Mossop, 1976, 1978a, b; Heymsfield and Mossop, 1984; Mossop, 1985a; Saunders and Hosseini, 2001), but to our knowledge, a negative control test excluding droplets smaller than around $12\ \mu\text{m}$ in

320 diameter was not conducted. The described correlation supported the hypothesis that spherical freezing might occur when a large droplet is accreted onto an already frozen small accreted droplet, leading to spherical freezing and ice shell fragmentation (Griggs and Choularton, 1983; Mossop, 1978a, 1985a). Although the influence of small droplets on rime-splintering can not be excluded, our observations indicate that a larger droplet accreting on a smaller ice structure on the rimer surface would spread instead of freezing as a spherical droplet. This is demonstrated by the case displayed in Fig. 10, where a droplet of $25\ \mu\text{m}$

325 diameter spreads over a narrow elevated ice structure with a characteristic length of $12\ \mu\text{m}$ at $-7\ ^\circ\text{C}$, rather than freezing spherically. Similar observations have been reported by Emersic and Connolly (2017) (Fig. 7a,b therein), where the spreading of two droplets with diameters of $30\ \mu\text{m}$ on a frozen droplet cap of about $11\ \mu\text{m}$ in diameter was observed at rimer temperatures of $-7\ ^\circ\text{C}$ to $-8\ ^\circ\text{C}$. Harris-Hobbs and Cooper (1987) presented a parameterization (HHC) relating the SIP rates and the droplet size distribution featuring droplets smaller than $13\ \mu\text{m}$ and larger than $24\ \mu\text{m}$ (flat DSD). This parameterization is based on

330 the results of HM-type experiments in support of the hypothetical mechanism of spherical freezing of larger droplets landing on top of smaller ones (Choularton et al., 1978, 1980). Since small droplets were present in only one of our experiments at $-5\ ^\circ\text{C}$, the HHC parameterization would have predicted no SIP or just a few particles for DSD2, which we, however, have not observed (see the reviewer comment by P. Connolly and our response). While we do not doubt the true nature of the correlation between the flat shape of the droplet size distribution and high SIP rates observed in the HM-type experiments, we have found

335 no evidence supporting the underlying physical mechanism. We thus conclude, that the correlation between the presence of small droplets and the high SIP rates in the HM-type experiments has to be based on a different physical mechanism, rather than a hypothetical spherical freezing of larger droplets landing on top of smaller droplets. Thus, the HHC parameterization is applicable only to the experiments that closely reproduce the HM-type SIP experimental settings and cannot be used for interpretation and even much less as an explanation of our negative results.

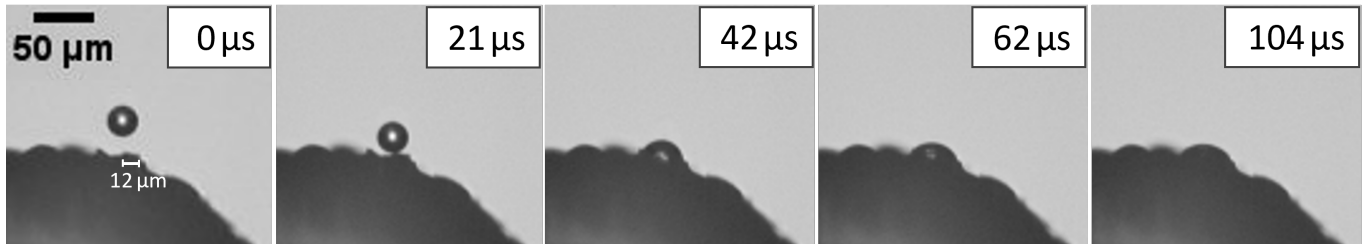


Figure 10. Counterexample to spherical droplet freezing on small ice structure. Collision of a $25\ \mu\text{m}$ in diameter droplet with a $12\ \mu\text{m}$ wide ice neck at $-7\ ^\circ\text{C}$ and $1\ \text{m s}^{-1}$.

340 (iii) The IDEFIX mass collision rates in dry growth regime are a factor 10 higher compared to those reported by Mossop (1985a). However, the characteristic time of individual droplet freezing is always much shorter than the characteristic inter-arrival time of colliding droplets (see Sect. 3.1). Thus, in the dry growth regime the rimer surface is completely frozen and in thermal equilibrium between the two consequent droplets colliding at the same site. From this point of view, the actual collision rate is not affecting the SIP efficiency as long as the growth regime remains dry. The accretion rate is only relevant
 345 for statistical quantification of the number of SI particles produced per mg rime.

(iv) In contrast to the HM-type experiments where droplets were produced by a steam generator, the humidified air flow in IDEFIX was slightly subsaturated with respect to ice. Therefore, no depositional growth of ice on the rimer surface could be observed. It should be noted, however, that for the frail ice structures (dendrites, needles, columns or prisms) to grow to the size where they could be detached upon collision with a droplet (Fig. 8d, II), a significant time is required. In the middle of the HM
 350 SIP temperature interval ($-5\ ^\circ\text{C}$) and at water saturation, an ice needle needs about 5 s to reach a length of $10\ \mu\text{m}$. During this time, the growing ice crystal would experience on average more than 10 collision events with a liquid droplet under IDEFIX conditions (see discussion in the section 3.1) and between 0 and 2 collisions in a former HM-type experiment (considering accretion rates given in Mossop, 1985a). Thus, an ice crystal growing via deposition of water vapor at water saturation has no chance to reach the size where it could be mechanically detached under IDEFIX experimental conditions, and only a slight
 355 chance under conditions present in the past HM-type experiments. Therefore, it remains an open question whether detachment of frail ice structures growing on the rimer surface via water vapor deposition could be an explanation for the high number of SI particles observed in the previous HM-type experiments as suggested by Mossop (1976). Note, however, that in a real atmospheric cloud, firstly, depositional ice growth is faster due to the lower gas pressure, and secondly, a falling graupel could experience strong variations of the accretion rate so that the frail ice structures might have time to develop.

360 We therefore conclude, that in spite of the difference between the experimental conditions of HM-type experiments and IDEFIX, the majority of the mechanisms (see points i to iii) supposedly underlying the effective SIP are not supported by our observations. The role of frail ice structures growing on the rimer surface via water vapor deposition remains an open question.

Previous HM-type experiments were limited to riming in the dry growth regime, because the formation of liquid layer during wet growth is thought to inhibit suitable conditions for rime-splintering (Pruppacher and Klett, 2010; Korolev and Leisner,
 365 2020). Interestingly, at $-5\ ^\circ\text{C}$ one of the equivocal cases indicating a potential SIP mechanism was observed during riming in

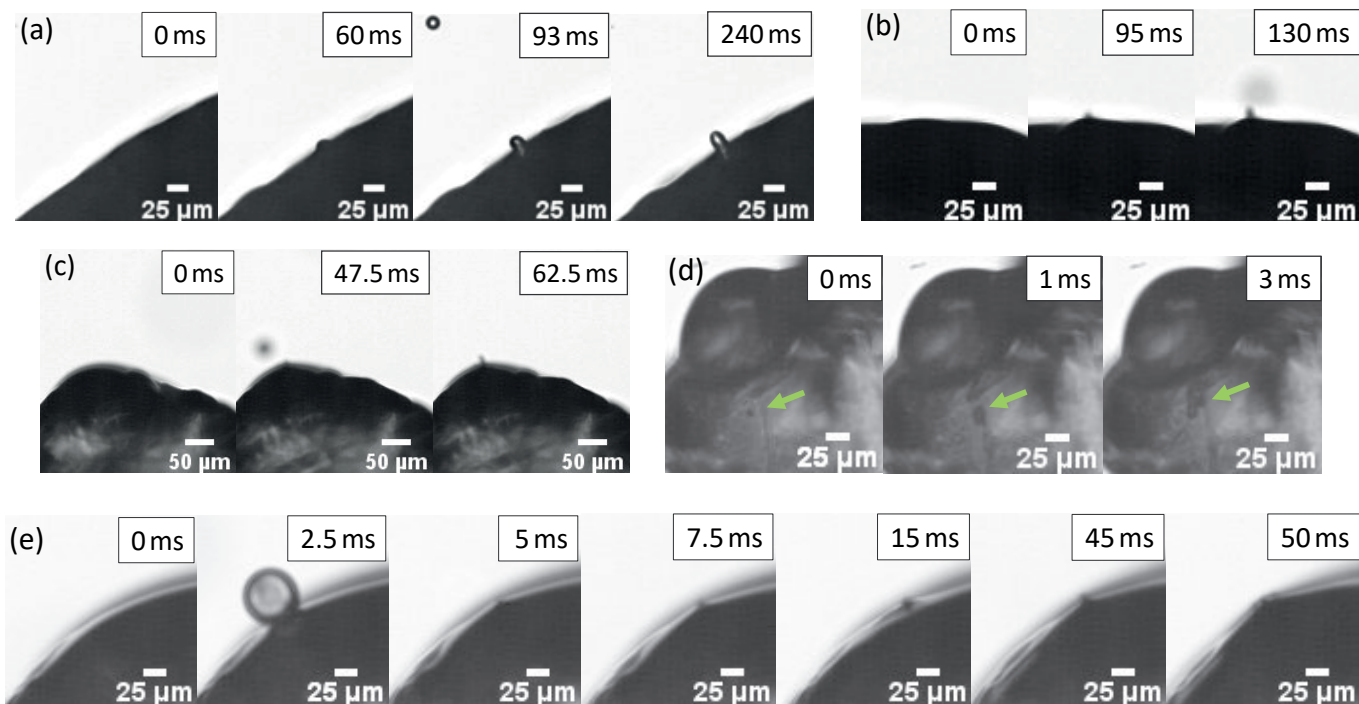


Figure 11. IDEFIX observations of ice spicule formation during transitional growth (a–c,e) and of ascending air bubbles within a liquid channel inside an ice target (d) at -10°C .

the transient growth regime. Occasionally, small ice spicules (about $20\ \mu\text{m}$ in length) were growing out of the freezing rimer surface after transition from wet to dry growth regime caused by fluctuation of collision rates at -10°C . Such ice spicule growth is illustrated in Fig. 11a–c,e. We hypothesize, that liquid water becomes entrapped in the pockets under the ice shell on the rimer surface during a change in growth regime from (local) wet to dry, causing internal pressure build-up and the spicule formation. Although no ice particles were detected in the IC in any of these cases, ice spicule formation could be a source of SI particles in analogy to SIP during freezing of large droplets. A similar case of spicule formation during wet growth has been described before only once in Macklin (1960). We have also observed gas bubbles appearing on the surface of ice shell of the frozen rimer after transition from wet to dry growth regime (Fig. 11d), indicating that the transient growth regime could be more important for rime-splintering SIP than previously recognized.

375

Rotation is required to form natural appearing graupel. In the IDEFIX experimental setup, the rimer is fixed by two crossing carbon fibers, excluding the random movement and precession that a natural graupel particle experiences during free fall. According to the time scale considerations given above, local microphysical processes on the rimer surface should not depend on the collision rate in the dry growth regime. Moreover, a free-falling graupel collects supercooled cloud droplets at the side which is exposed to airflow, similar to the IDEFIX conditions. It is also unlikely that the centrifugal force could cause break-off

380

of fragile structures. Jayaratne and Grigos (1991) have found that centripetal acceleration of 9 g are needed to break off the ice structures. This leads us to the conclusion that missing rotation or random movement has no influence on the rime-splintering mechanism per se.

4 Summary and conclusion

385 The Ice Droplets splintEring on FreezIng eXperiment (IDEFIX) has been designed to investigate the physical mechanisms underlying ice multiplication during riming of an ice particle falling through a cloud of supercooled droplets. In IDEFIX, the experimental conditions were selected to closely represent the environment within a mixed-phase convective cloud with respect to rimer size, ambient temperature, settling velocity and droplet size range. IDEFIX was focused on understanding the potential SIP mechanisms during riming on the microscopic scale, allowing for the observation of single droplet-ice accretion
390 events with high temporal and spatial resolution. To achieve this goal, the riming process was observed with high-speed video microscopy and IR thermography. The detection of SI particles was carried out using a custom-build ice counter based on the inertial deposition and subsequent growth of SI particles in a supercooled sucrose solution. Therewith, SI particles with initial diameters larger than approx. $3 \mu\text{m}$ could be reliably detected.

395 No evidence of a productive rime-splintering SIP was found during dry and wet graupel growth, in contrast to the reports on the previous HM-type experiments, where several hundreds of SI particles per mg rime were detected at -5°C . From our observations we conclude:

- Fragmentation of droplets freezing on top of smaller accreted droplets (Griggs and Choulaton, 1983) can most likely be ruled out as mechanism responsible for the effective ice multiplication during rime-splintering.
- 400 – Freezing of droplets upon glancing contact with the rimer (Mossop, 1976) was not observed.
- We found no indication of the SIP mechanisms associated with transient thermal gradient around a freezing droplet (King and Fletcher, 1976b; Dong and Hallett, 1989).
- Sublimational break-off of frail rime spires at -7°C and -10°C has been observed in the ice-subsaturated environment, but could not account for expected high numbers of SI particles under typical HM conditions (Hallett and Mossop, 1974).

405

The fact that the results from earlier HM-type experiments are not reproduced in this study can be explained in several ways. First, the number of SI particles observed in the earlier experiments could have been overestimated due to less controlled experimental conditions. This would imply that the HM SIP process is not as efficient in the mixed phase clouds as it has been assumed before. Second, the rime-splintering SIP can occur as random chain of rare burst events producing a high number
410 of SI particles, instead of being a continuous process producing low numbers of SI particles over the whole period of riming. A different type of experiment would be required to address this issue. Finally, the SI particles produced in IDEFIX could

be always significantly smaller than the detection limit of the ice counter (approx. $3\ \mu\text{m}$ in diameter). As IDEFIX is operated below ice-saturation, sub-micron ice particles would sublime completely or escape detection in the ice counter. This would imply that the actual SIP mechanism underlying the HM process could not be detected in IDEFIX. As sublimational break-off produces larger SI particles easily detectable in IDEFIX, and the spherical freezing of riming droplets and droplets freezing upon glancing contact with graupel could be excluded as potential mechanisms based on our observations, the nature of the alleged SIP mechanism behind the HM ice multiplication process remains unveiled.

In the transitional regime between dry and wet rimer growth (Schumann–Ludlam limit), pressure-induced rimer surface deformation has been observed. In analogy to droplets shattering upon freezing, such deformations could be indicative of SIP during pressure release events. Given that variation between high and low accretion rates might facilitate growth and sublimation of frail ice dendrites which could be detached upon collision with a droplet or ice particle, the role of temperature and humidity fluctuations in the clouds provides a new vantage point upon the rime-splintering ice multiplication mechanisms. At the very least, this observation points towards the possibility that rime-splintering SIP does not necessarily occur during riming in the dry growth regime only, as has been assumed so far. However, further experiments on riming at the Schumann–Ludlam limit would be needed to assess the frequency of surface deformation occurrence and its SIP-potential.

Summarizing, the number of ice crystals detected in IDEFIX experiments is much too low to explain the rapid glaciation observed in convective and frontal clouds. It is therefore likely, that other SIP mechanisms (review given in Korolev and Leisner, 2020) such as droplet shattering upon freezing, SIP due to ice-ice collisions, ice fragmentation during thermal shock, fragmentation during sublimation and activation of INP in transient super-saturation in the wake of a freezing droplet or hail have to be considered to explain the ice enhancement in mixed-phase clouds. In rapidly changing cloud conditions where no individual SIP mechanism can prevail for a long time, a combination or cascading chain of several SIP mechanisms is more likely to be the case.

Table A1. Impaction efficiency of different sized PSL particles was experimentally determined for different ice counter impactor nozzle diameters and volume flows. The corresponding theoretical particle cut-off diameter with 50% impaction efficiency based on the circular jet impaction model from Hinds (1999) are given.

nozzle diameter [mm]	volume flow [L min ⁻¹]	circular jet model $D_{p,50}$ [μm]	measured impaction efficiency of D_{PSL}			
			1.0 μm	2.0 μm	3.0 μm	4.5 μm
3.0	5.25	3.00	0	0.06	0.54	1.00
	6.75	2.76		0.16	0.62	
	8.24	2.50	0.08	0.25	0.66	
3.5	5.25	3.95		0.00	0.22	1.00
	6.75	3.48		0.00	0.52	1.00
	8.24	3.15		0.34	0.55	1.00
	12.35	2.57		0.5; 0.57		
4.0	6.75	4.21			0.27	
	8.24	3.82			0.38	
	12.35	3.10	0.13	0.39	0.76	1.00

Appendix A: Ice crystal detection limit

A1 Characterization of the Ice Counter

435 The IC is based on the principle of a conventional impactor (Kulkarni, 2011). To determine the impaction efficiency of particles
in the specifically designed IC, the theoretical particle aerodynamic cut-off diameter $D_{p,50}$ was derived by applying the circular
jet model (e.g., Hinds, 1999) and verified by additional characterization experiments. Particles larger than the $D_{p,50}$ tend to
impact on the substrate as their inertia causes them to escape the airflow, while particles smaller than the $D_{p,50}$ tend to follow
the streamlines of the air flow. In general, $D_{p,50}$ is defined as particle diameter at which particles impact with a probability of
440 50% and can be described as:

$$D_{p,50} = \sqrt{\frac{9\eta W Stk_{50}}{\rho_p C_c U}}, \quad (\text{A1})$$

with air viscosity η , nozzle diameter W , particle density ρ_p and Stokes number $Stk_{50} = 0.24$ (circular jet) corresponding to
 $D_{p,50}$ for $500 \leq Re \leq 3000$, slip correction C_c and jet velocity $U = \frac{Q}{\pi(\frac{W}{2})^2}$, and volumetric flow rate Q . C_c can be calculated
by $C_c = 1 + \frac{\lambda_g}{d_p} \left(2.34 + 1.05 \exp\left(-0.39 \frac{D_p}{\lambda_g}\right) \right)$, with λ_g the mean free path of air and particle diameter D_p . $D_{p,50}$ depends on
445 the nozzle diameter W with smaller nozzle diameters leading to smaller $D_{p,50}$. The IC has been constructed with the possibility
to exchange different nozzle diameters ($W = 3.0 \text{ mm}, 3.5 \text{ mm}, 4.0 \text{ mm}$). The theoretical description of $D_{p,50}$ is valid for particles
impacting on a solid plate. For the IDEFIX IC, a viscous aqueous solution is used as the impaction surface. The air flow is
directed perpendicular to the sugar solution and deforms the surface, which further complicates the theoretical description of
particle impaction. To overcome this difficulty, experiments with air-suspended monodisperse polystyrene latex particles (PSL

450 ranging from 1 μm to 4.5 μm) were conducted to measure the impaction efficiency for this setup for different air flow rates and nozzle diameters. PSL particles are guided either through the IC or through a bypass and the corresponding particle number concentration were measured with WELAS[®]. Then, the impaction efficiency of the IC is determined by dividing particle number concentration measured downstream the IC with particle number concentration of the bypass air flow. The results are summarized in Table A1. Verification experiments showed that the essential behavior is represented by the theoretical model.

455 In detail, experimentally determined $D_{p,50}$ values are smaller than the theoretical description, resulting in a better collection efficiency for this specific setup of the IC.

A2 Sublimation of secondary ice particles in IDEFIX

The impaction characteristics of particles in the IC and sublimational effects limit the detectable size of SI particles. At the current configuration of IDEFIX, SI particles with 3.3 μm in diameter would shrink to 2 μm on their pathway into the IC

460 considering the worst case scenario of saturation conditions with respect to ice (Fig. A1). With this, such particles will be impacted in the IC with an efficiency of 50%. If SI particles have smaller diameters than 3.3 μm at their production, the probability that they will be counted within the IC decreases significantly. Therefore, this size is assumed to be the lower detection limit.

Appendix B: Determination of the collision rates during riming

465 B1 Methods

Droplet-graupel collision rates influence rimer microphysical processes and are relevant statistical parameters to describe SIP rates. Hence, they are crucial parameters for the comparability to other rime-splintering experiments. The collision rates can be expressed in terms of mass and number of accreted supercooled droplets, respectively. For reasons of comparability, the collision rates are normalized to the graupel's geometrical cross sectional area perpendicular to the flow direction (A_{cross}).

470 An average mass collision rate, also called mass accretion rate ($R_{\text{accr},M}$) in the following, can be calculated from the frozen droplet mass accreted on the initial ice target (ΔM_{accr}) in a certain time interval (Δt):

$$R_{\text{accr},M} = \frac{1}{A_{\text{cross}}} \frac{\Delta M_{\text{accr}}}{\Delta t}. \quad (\text{B1})$$

To derive the number accretion rate, the mass accretion rate (Eq. B1) is divided by the mean mass of the number size distribution of the accreted droplets $\langle M_d \rangle = \frac{\pi}{6} \rho_w \frac{M_3}{M_0}$, with M_0 and M_3 being the 0th and 3rd moment of the distribution

475 $n_{\text{accr}}(D)$. From additional WELAS[®] measurements, the airborne droplet number size distribution $n(D)$ is found to be log-normal distributed. Since the normalized size distribution of airborne droplets $n^*(D) = \frac{n(D)}{M_0} = \frac{n(D)}{\int n(D') d \log D'}$ is not influenced by riming, i.e. the shape of the normalized DSD does not change comparing measurements without and with an ice target (Fig. B1), we assume $n^*(D)$ to represent the normalized accreted DSD and the following is obtained

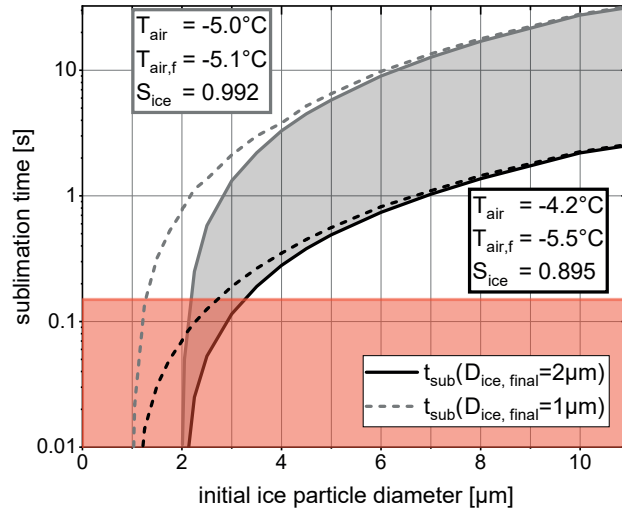


Figure A1. Sublimation time as a function of initial ice particle diameter. Ice particles are assumed to have a spherical shape and experience different levels of subsaturation with respect to ice. The time it takes to sublimate to a final ice particle size of $D_{ice,final} = 2 \mu\text{m}$ (solid lines, light gray shaded area) and $1 \mu\text{m}$ (dashed lines) are shown since they correspond to expected IC counting efficiencies of 50 % and significant below 50 %, respectively. Two extreme scenarios span the relevant parameter space regarding temperature T , frost point T_f and respective saturation with respect to ice S_{ice} representative for an IDEFIX experiment, i.e., almost ice saturation (gray line) at set temperature and 90 % saturation accounting for temperature and humidity uncertainties (black line). The residence time from ice target to supercooled sugar solution surface is given (red line). When sublimation time is shorter than residence time (red area), ice particles are detected with less than 50 % for $D_{ice,final} = 2 \mu\text{m}$ and might be too small to be detected for $D_{ice,final} = 1 \mu\text{m}$.

$$R_{accr,N} = \frac{R_{accr,M}}{\langle M_d \rangle} = \frac{6}{\pi \rho_w} \int D'^3 n^*(D') d \log D' R_{accr,M}. \quad (\text{B2})$$

480 Currently, the IDEFIX setup does not allow a direct measurement of the ice target weight before and after riming. To determine the mass accretion rate for a representative set of experiments, the increase of rimer mass in a certain time interval Eq. (B1) was derived via two different and mostly independent methods using a) 2D information from HSV images, and b) the rimer surface temperature from IR thermography as input parameter for a heat balance model of graupel adopted from Pruppacher and Klett (2010).

485 Considering the first method, the accreted mass per time period was estimated from the projected rimer surface area as seen on the HSV images (Fig. B2). Since the ice target is attached to a cross of carbon fibers and therefore has no rotational degree of freedom, the riming occurs only on the upper part of the ice target. Neglecting microscopic rimer surface structure, the projected area of the rimer in matured stage was observed to take on a semi-ellipsoidal shape. Using the freely accessible image analysis tool imageJ, the respective half width b_2 and height h_2 are determined (Fig. B2, right). In doing so, the half ellipse was adjusted to be fully within the visible graupel area of the HSV image. The volume increase due to accretion of

490

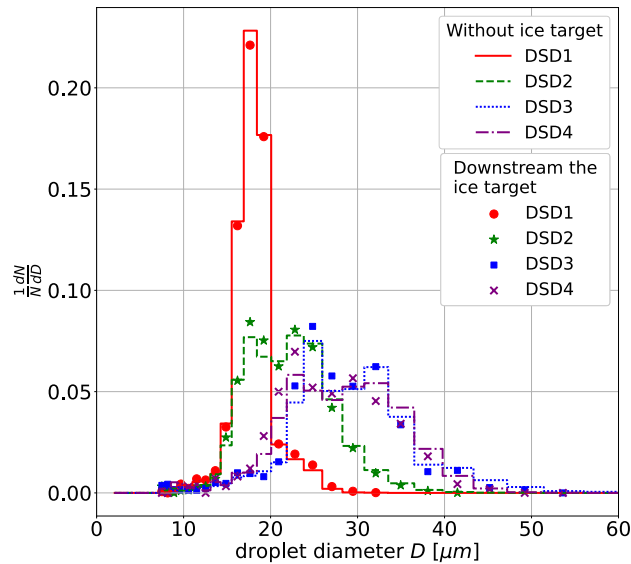


Figure B1. Measurements of the droplet size distributions DSD1-4 without (lines) and downstream (symbols) an ice target at $-5\text{ }^{\circ}\text{C}$ and 1 m s^{-1} .

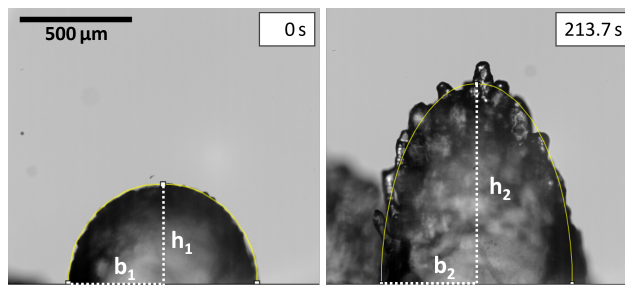


Figure B2. HSV-images showing a nearly spherical ice target before (left) and more ellipsoidal shaped ice target during riming (right). In this example droplets of DSD2 are accreted on the fixed ice target with an air flow velocity of 1 m s^{-1} at $-5\text{ }^{\circ}\text{C}$. The adjusted semi-ellipse of the rimer top is depicted in yellow together with the two half-axes of the semi ellipse: height h and width b .

droplets observed between two different time steps is calculated assuming rotational symmetry and subtracting the determined ice target volumes. Following this approach, the uncertainty results either from air cavities within the rimer body or rime spire structures that are grown beyond the ellipsoid and is assumed to be approx. 10% in volume. To obtain the accreted rimer mass from the derived volume increase, a rimer density was assumed.

495

Via the second method, the mass accretion rates were calculated by applying the heat balance model of a riming particle given in Pruppacher and Klett (2010) using the rimer surface temperature from infrared thermography as input data. Assuming steady state conditions and a constant surface temperature, the heat q and mass m transfer at a riming ice particle becomes

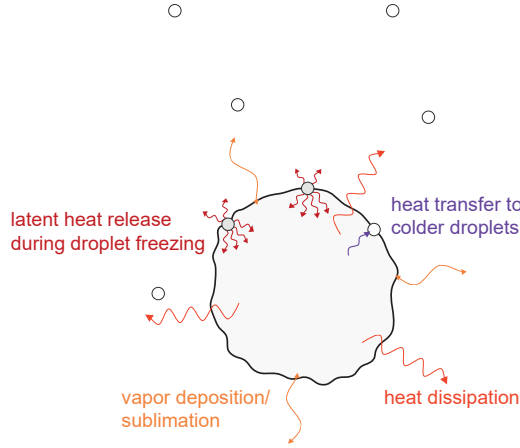


Figure B3. Schematics of the relevant heat transfer of a riming ice particle.

simplified to Eq. (B3) (Pruppacher and Klett, 2010, p. 680-681).

$$500 \quad \left(\frac{dq}{dt}\right)_{\text{diff,h}} + \left(\frac{dq}{dt}\right)_{\text{diff,m}} + \left(\frac{dq}{dt}\right)_{\text{accr}} + \left(\frac{dq}{dt}\right)_{\text{fr}} = 0 \quad (\text{B3})$$

The contributing terms to the riming heat balance, illustrated in Fig. B3, are (i) the heat dissipation to the environment:

$$\left(\frac{dq}{dt}\right)_{\text{diff,h}} = -\frac{A_{\text{tar}}k_aNu(T_{\text{tar,s}} - T_{\text{env}})}{D_{\text{tar}}} \quad (\text{B4})$$

with target surface area A_{tar} and target diameter D_{tar} , thermal conductivity of dry air k_a (param. in Beard and Pruppacher, 1971), Nusselt number $Nu = 0.88Re^{\frac{1}{2}}Pr^{\frac{1}{3}}$ including Reynolds Re and Prandtl Pr number, temperature of the ice target
505 surface $T_{\text{tar,s}}$ and of the humid air environment T_{env} ; (ii) heating rate due to vapor deposition or sublimation:

$$\left(\frac{dq}{dt}\right)_{\text{diff,m}} = L_s \left(\frac{dm}{dt}\right)_{\text{diff}} \quad (\text{B5})$$

with latent heat of sublimation L_s (param. in Murphy and Koop, 2005) and diffusional growth term, which can be written as

$$\left(\frac{dm}{dt}\right)_{\text{diff}} = \frac{A_{\text{tar}}D_vM_wNu}{D_{\text{tar}}R^*} \left(\frac{e_{\text{env}}}{T_{\text{env}}} - \frac{e_{\text{tar,s}}}{T_{\text{tar,s}}}\right) \quad (\text{B6})$$

including diffusivity of water vapor in air D_v (param. in Hall and Pruppacher, 1976), molar weight of water $M_w = 0.01801 \text{ J kg}^{-1}$,
510 ideal gas constant $R^* = 8.31446 \text{ J mol}^{-1} \text{ K}^{-1}$, temperature and water vapor partial pressure over ice of the environment
(T_{env} , e_{env}) and target surface ($T_{\text{tar,s}}$, $e_{\text{tar,s}}$), respectively; (iii) heating rate to warm accreted droplets:

$$\left(\frac{dq}{dt}\right)_{\text{accr,h}} = -c_w(T_{\text{tar}} - T_{\text{env}}) \left(\frac{dm}{dt}\right)_{\text{accr}} \quad (\text{B7})$$

with heat capacity of supercooled water c_w (Biddle et al., 2013) and mass accretion rate $\left(\frac{dm}{dt}\right)_{\text{accr}}$ and finally, (iv) latent heat release due to freezing of accreted droplets

$$515 \quad \left(\frac{dq}{dt}\right)_{\text{fr}} = L_f \left(\frac{dm}{dt}\right)_{\text{accr}} \quad (\text{B8})$$

with the latent heat of fusion L_f (Pruppacher and Klett, 2010, p.97) and the mass accretion rate $\left(\frac{dm}{dt}\right)_{\text{accr}}$ to be determined, which describes the mass increase per time interval due to accretion of colliding and subsequent freezing supercooled droplets during riming. Solving the rimer heat balance equation (Eq. B3) for the mass growth rate due to droplet accretion $\left(\frac{dm}{dt}\right)_{\text{accr}}$ results in the following expression:

$$520 \quad \left(\frac{dm}{dt}\right)_{\text{accr}} = \frac{-\left(\frac{dq}{dt}\right)_{\text{diff,h}} - \left(\frac{dq}{dt}\right)_{\text{diff,m}}}{L_f - c_w(T_{\text{tar,s}} - T_{\text{env}})} \quad (\text{B9})$$

To describe the rimer surface area, the graupel was assumed to compose of a half sphere at the bottom and a rotation-symmetric semi-ellipsoid on top. The graupel diameter and the height of the semi-ellipsoid were determined in analogy to the first method. Applying the heat-balance model to calculate the mass accretion rate, it must be distinguished between dry and wet growth conditions. Eq. B9 is valid for riming in the dry growth regime. During wet growth, the surface temperature
525 increases to the melting point enabling liquid layer formation on the rimer top and thus, $\left(\frac{dq}{dt}\right)_{\text{diff,m}}$ is a function of latent heat of evaporation instead of sublimation and the water vapor partial pressure at the target surface is considered over water instead of over ice. To get an idea of the scales of the terms contributing to the heat balance equation (Eq. B3), which is the basis for Eq. B9, the individual terms were calculated for the examples of dry, wet, and transition growth presented in Fig. 4, Sect. 3.1 and are given in Table B1.

Table B1. Heat balance of a riming ice particle for three examples of dry, wet and transitional growth (Fig. 4a,b,c). The surface temperature elevation is applied as input parameter to calculate the contributions of the different heat fluxes.

growth regime	dT [K]	$\left(\frac{dq}{dt}\right)_{\text{fr}}$ [mW]	$\left(\frac{dq}{dt}\right)_{\text{diff,h}}$ [mW]	$\left(\frac{dq}{dt}\right)_{\text{diff,m}}$ [mW]	$\left(\frac{dq}{dt}\right)_{\text{accr}}$ [mW]
dry (C2_T39)	0.6	0.33	-0.21	-0.11	-0.00
wet (C2_T56)	4.94	3.34	-1.87	-1.32	-0.21
transition (C2_T50)					
dry limit	5.03	7.32	-4.62	-2.50	-0.50
wet limit	8.03	12.16	-7.37	-4.11	-1.32

530 B2 Number and mass collision rates

Both independent methods described in Sect. B1 were used to derive the collision rates in dependence of the DSD for a subset of experiments at different thermodynamic conditions. The compilation of number and mass collision rates determined from methods (a) and (b) is presented in Fig. B4.

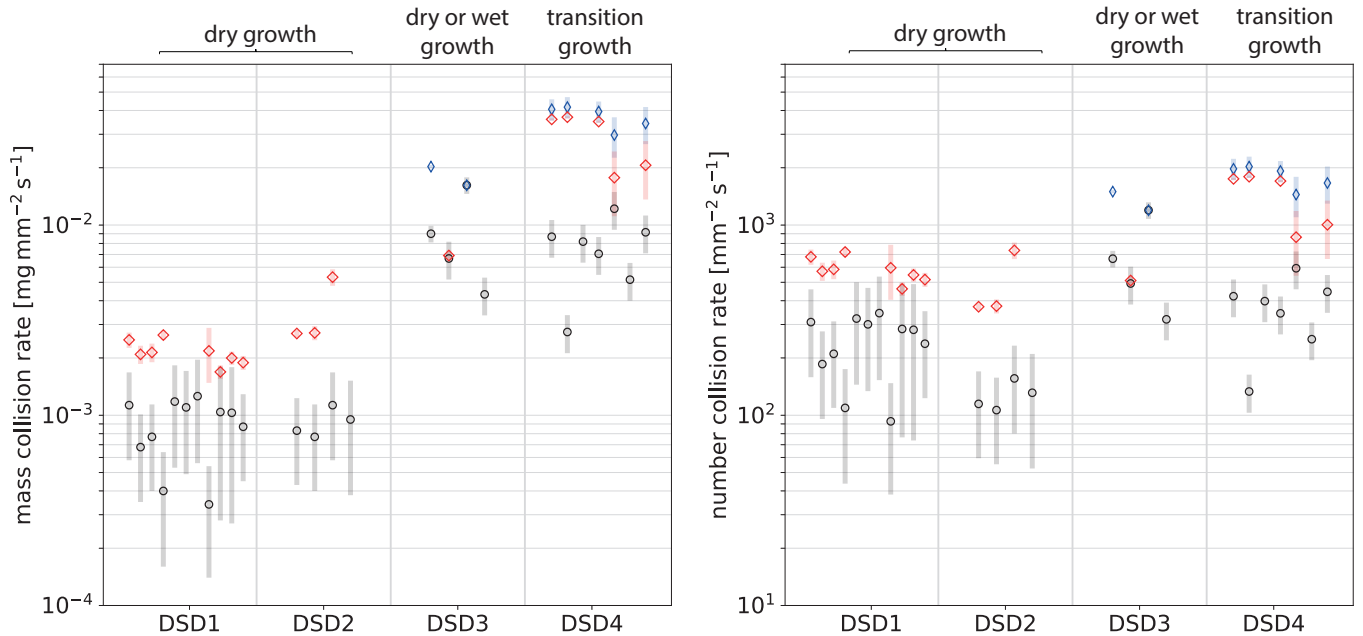


Figure B4. Mass and number collision rates grouped by droplet size distributions DSD1–4 and correspondingly observed growth regime. Average collision rates derived each via method (a) (black open circles) and method (b) based on the heat balance model assuming either a frozen ice target surface (dry growth conditions, red open diamonds) or a liquid water surface (wet growth conditions, blue open diamonds) depending on case. For the transition regime resulting from DSD4, the HSV-image based collision rates represent an average value accounting for the relevant ice density range (gray shaded bars), while applying the heat-balance method an upper (considering wet growth) and lower (considering dry growth) range is given.

Using 2D information from HSV images (method a), the following input parameter are applied. In addition to diameter
 535 and height of the rimed ice target, the graupel density is needed to calculate the accreted rimer mass (Eq. B1,B2). In general, the graupel density can vary greatly depending on formation conditions. Due to the fact, that the graupel density and thus the volume of air cavities within the graupel structure can not be determined at the IDEFIX experiments, a density of 0.9 g m^{-3} , corresponding to compact ice without any air spaces, is assumed as an upper limit. Parameterizations of graupel density from Cober and List (1993) and Heymsfield and Pflaum (1985), where it is a function of the rimer surface temperature, the impact
 540 velocity and the median radius of the accreted cloud droplets (Macklin, 1962), are applied as lower limit. The mean values and the possible range according to variable rimer densities are represented as symbols and gray shaded bars in Fig. B4, respectively. The number collision rates are obtained by accounting for the respective DSDs.

Applying method (b) – the determination of mass and number accretion rate derived from the heat balance model according to Pruppacher and Klett (2010) – steady state conditions can be assumed as the rimer surface temperature increases to a
 545 constant value in first approximation (see Sect. 3.1). Therefore, Eq. (B9) is easy to solve and inserted into Eq. (B1). The surface temperature elevation during riming derived from infrared thermography, target diameter and rimer surface area determined

from HSV images are applied as input parameter. Thereby, it is discriminated between the dry and wet graupel growth regime by accounting for the respective properties of the ice or liquid water surface in Eq. (B9). For transitional growth (alternating ice and liquid water surface) both growth regimes are applied. Due to an inhomogeneous distribution of the surface temperature, the collision rates are calculated by using the average surface temperature displayed as symbol in Fig. B4 and the range of surface temperature variation is represented as bars.

Droplet-rimer collisions of DSD1 and DSD2 result in average number and mass collision rates of $3.6 \times 10^2 \text{ mm}^{-2} \text{ s}^{-1}$ and $1.6 \times 10^{-3} \text{ mg mm}^{-2} \text{ s}^{-1}$, respectively. For DSD3 and DSD4 the respective average number and mass collision rates are higher with $8.7 \times 10^2 \text{ mm}^{-2} \text{ s}^{-1}$ and $1.6 \times 10^{-2} \text{ mg mm}^{-2} \text{ s}^{-1}$, respectively, enabling the transition to wet growth. Comparing the approaches, method (b) results almost always in a factor of 2 to 4 times higher accretion rates than method (a) independently of the applied droplet size distribution. A possible reason for the discrepancy between the results of both methods is probably the simplified assumption of the ice target surface. However, it is remarkable that two independent approaches achieve nearly similar collision rates.

To assess the atmospheric relevant parameter space of number and mass accretions rates during riming for different cloud convection types, there are almost no atmospheric observations available. From ground-based observations and theoretical considerations, Erfani and Mitchell (2017) derived mass collision rates on the order $10^{-5} \text{ mg mm}^{-2} \text{ s}^{-1}$ for frontal clouds considering liquid water contents (LWCs) from 0.05 g m^{-3} to 0.2 g m^{-3} and cloud droplets of median mass diameter $8 \mu\text{m}$ and $16 \mu\text{m}$. Jensen and Harrington (2015) simulated similar mass collision rates of $2\text{--}5 \times 10^{-5} \text{ mg mm}^{-2} \text{ s}^{-1}$ for LWC of 0.3 g m^{-3} and droplet mean diameter between $10 \mu\text{m}$ and $24 \mu\text{m}$. Since the estimated LWC and the mass accretion rates in the IDEFIX experiments are at least two orders of magnitude above this, it can be assumed that the riming conditions at IDEFIX are more representative for convective clouds.

Appendix C: Melting point calibration of IR camera

In the experiments in which wet graupel growth could be observed with the HSV camera due to the visible formation of liquid layers on top of the rimer surface, the IR-measured maximum of the surface temperature during riming was not reaching 0°C , but appearing between -1°C and -2°C . To check, whether the measured temperature maximum corresponds to the physical melting point of water, a calibration was done. Therefore, a spherical target made from epoxy resin adhesive was inserted into the IDEFIX chamber and a cap of liquid water with roughly diameter of $0.5\text{--}1 \text{ mm}$ was generated on the top of it. Ice crystals were then inserted into the chamber by putting the tip of a screwdriver covered with ice (it was shortly dipped into liquid nitrogen) through one of the corona needle slots into the head section of IDEFIX. Once the liquid cap was hit by an ice crystal, the freezing was initiated and the rapid spread of dendritic ice structures over the liquid could be captured with the HSV camera. From parallel surface temperature monitoring of the IR camera, we obtained a surface temperature maximum of $-1.4 \pm 0.6 \text{ K}$ (average of three experiments, uncertainty range of 3σ) in the moment of freezing, where the liquid cap physically should have a temperature of 0°C .

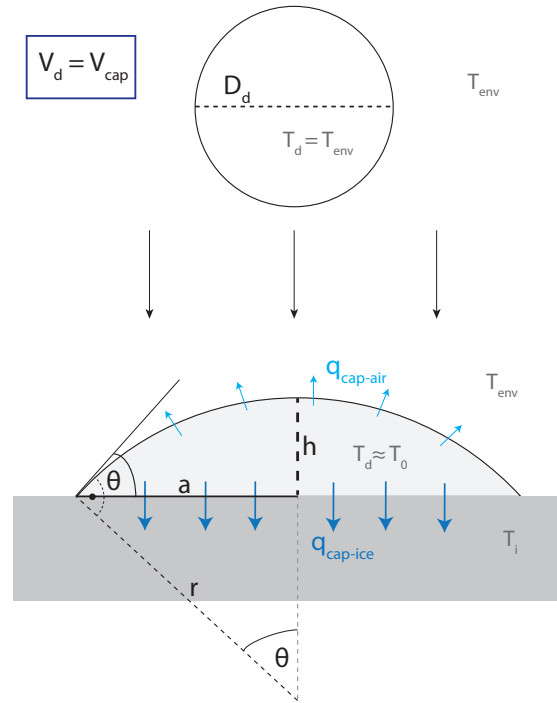


Figure D1. Geometry of a supercooled droplet ($T_d < T_0 = 273.15$ K) of diameter D resulting in a freezing spherical cap with contact angle θ , base radius a , height h and radius of the imaginary sphere r on an ice surface of temperature T_i after collision. Heat released during the freezing process of the droplet water is transferred to the environmental air ($q_{\text{cap-air}}$) of temperature T_{env} and to the ice surface ($q_{\text{cap-ice}}$).

Appendix D: Freezing and inter-arrival time of accreted droplets on ice surface

580 To calculate the individual freezing time and the inter-arrival time of two consecutive droplets hitting the same site, we consider the following system (Fig. D1): a supercooled droplet with a diameter of D_d and a volume of V_d in an air stream is assumed to have the same temperature as the environment $T_d = T_{\text{env}}$. After collision with the large rimer surface, the supercooled water droplet forms a spherical liquid cap with contact angle θ at the water-air-ice interface (observation described in Sect. 3.1) and radius $a = r \sin \theta$ whereby r is the radius of the imaginary sphere. During freezing, the temperature of the spherical cap rises

585 to the melting point of water $T_d = T_0 = 273.15$ K. The freezing time of the droplets can be approximated with the time of the second freezing stage, since the initial freezing and the adaptation to the ambient temperature after freezing happen on a much smaller time scale and are therefore negligible (Pruppacher and Klett, 2010; Korolev and Leisner, 2020).

The freezing time t_2 is determined by the transfer of latent heat to the surrounding air $q_{\text{cap-air}}$ and the ice body $q_{\text{cap-ice}}$. Solving the heat balance equation for a ventilated spherical droplet cap on an ice substrate according to Macklin and Payne

590 (1968) (cited in Pruppacher and Klett, 2010) and allowing for a variable contact angle yields

$$\alpha t_2 + \beta \sqrt{t_2} - \gamma = 0 \quad (\text{D1})$$

with

$$\alpha = 2\pi \frac{D_d \sin \theta}{(2(2 + \cos \theta)(1 - \cos \theta)^2)^{\frac{1}{3}}} \bar{f} [k_a (T_0 - T_{\text{env}}) + L_e D_v (\rho_{v,a} - \rho_{v,\text{env}})],$$

$$\beta = (T_0 - T_{\text{cap}}) k_i \frac{D_d^2 (\sin \theta)^2}{(2(2 + \cos \theta)(1 - \cos \theta)^2)^{\frac{2}{3}}} \sqrt{\frac{\rho_i c_i \pi}{k_i}},$$

$$595 \quad \gamma = -\frac{\pi}{6} D_d^3 \rho_w [L_f - c_w (T_0 - T_{\text{env}})],$$

The analytical solution for t_2 is

$$t_2 = \left(\frac{-\beta + \sqrt{\beta^2 - 4\alpha\gamma}}{2\alpha} \right)^2. \quad (\text{D2})$$

Thereby $q_{\text{cap-air}} = \alpha t_2$ and $q_{\text{cap-ice}} = \beta \sqrt{t_2}$. γ is the total amount of released heat. \bar{f} is the mean ventilation coefficient ($\bar{f} = 1.5$), k_a represents the thermal conductivity of dry air (param. in Beard and Pruppacher, 1971; Pruppacher and Klett, 600 2010, p. 508). k_i is the thermal conductivity of ice (param. in Pruppacher and Klett, 2010, p. 676). L_e and L_f are the latent heats of evaporation and freezing (param. in Pruppacher and Klett, 2010, p. 97), respectively. Further, the diffusivity of water in air D_v (param. in Pruppacher and Klett, 2010, p. 503), the water vapor densities of air at the cap surface $\rho_{v,a}$ and in the distant environment $\rho_{v,\text{env}}$, the density of liquid water ρ_w (param. in Hare and Sorensen, 1987; Pruppacher and Klett, 2010, p. 87) and ice ρ_i (param. in Baron and Willeke, 2001), the heat capacity of liquid water a c_w (param. in Biddle et al., 2013) and 605 ice c_i (param. in Pruppacher and Klett, 2010, p. 87) are considered.

In addition to the individual droplet freezing time, the inter-arrival time is also relevant for the understanding of micro- and macroscopical rimer structure in the different growth regimes. Based on the number collision rate, it is possible to estimate the statistical inter-arrival time (t_i) between two droplets colliding at the same site on the rimer surface via Eq. D3. Both droplets are considered to form spherical caps upon accretion with base area A_{cap} .

$$610 \quad t_i = \frac{1}{R_{\text{accr},N} A_{\text{cap}}} \quad (\text{D3})$$

The inter-arrival time is an important parameter for developing rimer surface structure during riming, as described in Sect 3.1.

Appendix E: Rime-splintering experiments at IDEFIX

A detailed overview of all valid rime-splintering experiments comprising the parameter space and observations of riming, SIP and other features is given in Table E1. The few cases, where potential SI particles were detected in the IC during or after 615 riming, are illustrated in Fig. E1 with a pair of a HSV and IC images showing the matured rimer structure and detected ice crystals.

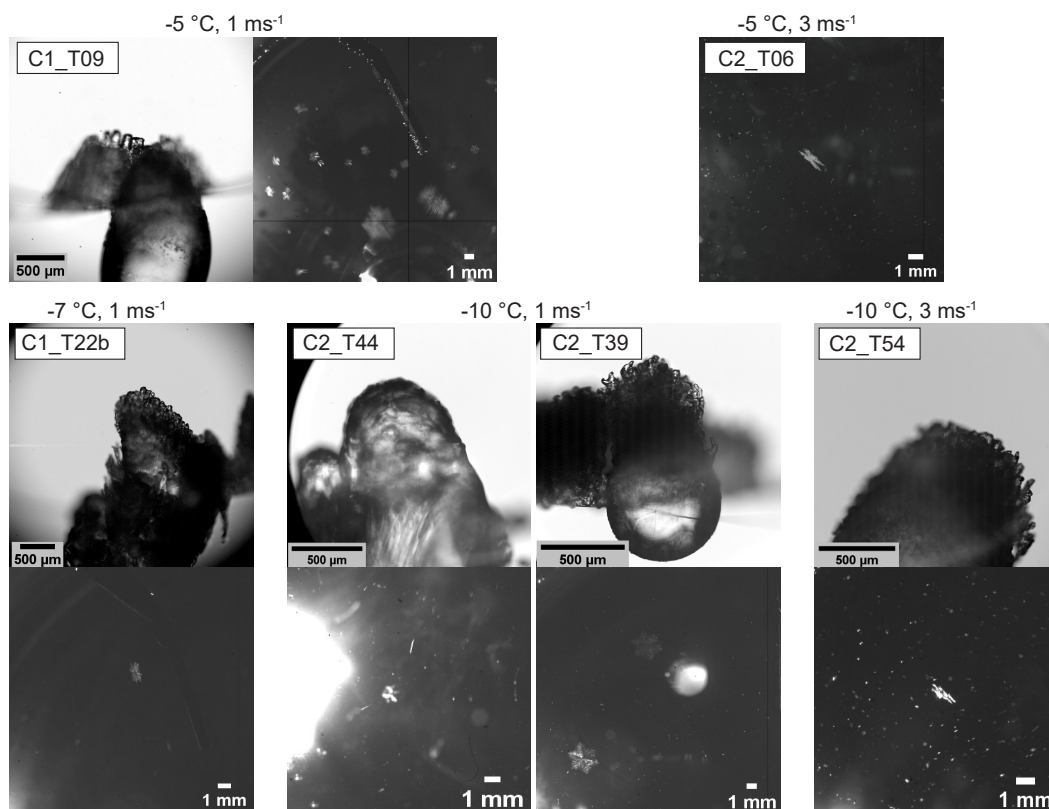


Figure E1. HSV images illustrating the rimed structure of ice targets from experiments in which SIP particles have been detected with the IC together with the corresponding enlarged cut-out of an IC image showing detected ice crystals close to the end of the experiment. A HSV image of C2_T06 is missing due to lack of HSV data.

Table E1. Overview of valid rime-splintering experiments in dependence on the main parameters: set air temperature, air velocity, droplet size distribution (DSD). The accreted mass is mainly determined by using HSV method (described in Sect. B1) or * calculated from average mass collision rate and riming time. The validation criteria comprised general functionality tests of the ice counter as well as ice counter background tests before and after each riming experiment and a minimum of approximately 0.1 mg of total accreted rime mass during the experiment. ** in this case, DSD2 was initially unstable and periods of more collisions and larger droplets occurred briefly, leading to local wetting of the ice surface.

T [°C]	u_{\max} [m s ⁻¹]	experiment	DSD	growth regime	total accreted mass [mg]	ice detected, number of crystals	ice particle occurrence, special observations
-4	1	C2_T34	DSD1	dry	0.1–0.2	no	
		C2_T38	DSD1	dry	0.1*	no	
		C2_T35	DSD2	dry	0.1–0.2	no	
		C2_T38b	DSD3	wet	0.1–0.2*	no	
-5	1	C1_T09	DSD1	dry	0.2–0.3*	yes, >20	during riming
		C1_T12	DSD1	dry	0.1–0.2	no	
		C1_T13	DSD1	dry	0.2–0.3	no	
		C1_T20	DSD1	dry	0.1–0.2	no	
		C2_T59	DSD1	dry	0.1–0.2	no	
		C2_T57	DSD2	dry	0.1–0.2	no	
		C2_T56	DSD3	wet	0.2	no	
	3	C2_T04	DSD1	dry	0.4–0.6	no	
		C2_T04b	DSD3	dry	0.1–0.8*	no	
		C2_T06	DSD3	dry/transition	0.5–1.4*	yes, 5	during riming
6	C2_T60	DSD1	dry	0.1	no		
-7	1	C1_T22	DSD1	dry	0.2–0.4	no	
		C2_T15	DSD1	dry	0.1	no	
		C2_T19	DSD1 & DSD2 varied	dry	0.1–0.2	no	
		C2_T20	DSD1 & DSD2 varied	dry	0.2–0.5	no	
2	C1_T22b	DSD1	dry	0.1–0.2	yes, 1	after riming (rime spire break-off)	
3	C2_T12	DSD1	dry	0.1–0.2*	no		
-10	1	C2_T39	DSD1	dry	0.1*	yes, 2	after riming
		C2_T43	DSD1	dry	0.1–0.3	no	
		C2_T40	DSD2	dry	0.1*	no	
		C2_T45	DSD2	dry, initially unstable**	0.1*	no	ice spicule growth during riming (Fig. 11c)
		C2_T44	DSD4	transition	0.1–0.2	yes, 1	after riming, ice spicule growth during riming (Fig. 11e)
		C2_T48	DSD4	transition	1.3	no	ice spicule growth during riming (Fig. 11a,b)
		C2_T50	DSD4	transition, dry	0.4–0.5	no	ascending air bubbles (Fig. 11d)
3	C2_T54	DSD1	dry	0.1–0.2	yes, 1	after riming (rime spire break-off)	
	C2_T53	DSD3	dry	0.5–0.7*	no		

Data availability. All data can be requested from the authors. Data sets comprising the IDEFIX droplet size distributions and the overview table of valid experiments are available on Zenodo with <https://doi.org/10.5281/zenodo.8405273>.

Video supplement. HSV sequences are stored on Zenodo and can be accessed via <https://doi.org/10.5281/zenodo.8405453>.

620 *Author contributions.* JS and SH wrote the paper with contributions from all co-authors, the concept of the study was developed by SH, AK, AAK, TL and FS. The measurements and data analysis and theoretical considerations were done by JS, SH and supported by AK, AAK and FS. SH and AAK acquired the funding.

Competing interests. The authors declare no competing interests.

Acknowledgements. SH gratefully acknowledge the funding by the German Research Foundation (project number HA 8322/1-1). AK and
625 AAK acknowledge DFG funding (project number KI 1997/1-1). AAK and TL acknowledge financial support by the Helmholtz Association under Atmosphere and Climate Programme (ATMO). AK and AAK are thankful to Stephan Vogt (IMK-AAF) for designing the the ice counter. SH and JS are very thankful to Silvio Schmalfuß and Jens Voigtländer for supporting the model simulation to design IDEFIX, Astrid Hofmann, Bruno Wetzl and Thomas Conrath for supporting the construction, and Stephan Mertes, Dennis Niedermeier for fruitful discussions and providing TDL and dew point instruments, respectively. We also thank the reviewer Paul Connolly for a fruitful discussion and his additional
630 coding work.

References

- Aufdermaur, A. N. and Johnson, D.: Charge separation due to riming in an electric field, *Quart. J. Roy. Meteorol. Soc.*, 98, 369–382, 1972.
- Bacon, N. J., Swanson, B. D., Baker, M. B., and Davis, E. J.: Breakup of levitated frost particles, *J. Geophys. Res.-Atmos.*, 103, 13 763–13 775, <https://doi.org/10.1029/98jd01162>, 1998.
- 635 Bader, M., Gloster, J., Brownscombe, J., and Goldsmith, P.: The production of sub-micron ice fragments by water droplets freezing in free fall or on accretion upon an ice surface, *Quart. J. Roy. Meteorol. Soc.*, 100, 420–426, 1974.
- Baron, P. A. and Willeke, K.: *Aerosol fundamentals, Aerosol measurement: principles, techniques, and applications*, 2, 2001.
- Beard, K. and Pruppacher, H. R.: A wind tunnel investigation of the rate of evaporation of small water drops falling at terminal velocity in air, *J. Atmos. Sci.*, 28, 1455–1464, 1971.
- 640 Biddle, J. W., Holten, V., Sengers, J. V., and Anisimov, M. A.: Thermal conductivity of supercooled water, *Phys. Rev. E*, 87, 042 302, 2013.
- Bigg, E. K.: A new Technique for Counting Ice-Forming Nuclei in Aerosols, *Tellus*, 9, 394–400, <https://doi.org/https://doi.org/10.1111/j.2153-3490.1957.tb01895.x>, 1957.
- Brownscombe, J. L. and Hallett, J.: Experimental and field studies of precipitation particles formed by the freezing of supercooled water, *Quart. J. Roy. Meteorol. Soc.*, 93, 455–473, <https://doi.org/https://doi.org/10.1002/qj.49709339805>, 1967.
- 645 Chisnell, R. and Latham, J.: Ice particle multiplication in cumulus clouds, *Quart. J. Roy. Meteorol. Soc.*, 102, 133–156, 1976.
- Choulaton, T., Griggs, D., Humood, B., and Latham, J.: Laboratory studies of riming, and its relation to ice splinter production, *Quart. J. Roy. Meteorol. Soc.*, 106, 367–374, 1980.
- Choulaton, T. W., Latham, J., and Mason, B. J.: Possible mechanism of ice splinter production during riming, *Nature*, 274, 791–792, <https://doi.org/10.1038/274791a0>, 1978.
- 650 Cober, S. G. and List, R.: Measurements of the heat and mass transfer parameters characterizing conical graupel growth, *J. Atmos. Sci.*, 50, 1591–1609, 1993.
- Connolly, P.: Referee Comment on egosphere-2023-2891, <https://doi.org/https://doi.org/10.5194/egosphere-2023-2891-RC2>, 2024.
- Connolly, P. J., Heymsfield, A. J., and Choulaton, T. W.: Modelling the influence of rimer surface temperature on the glaciation of intense thunderstorms: The rime–splinter mechanism of ice multiplication, *Quart. J. Roy. Meteorol. Soc.*, 132, 3059–3077, <https://doi.org/10.1256/qj.05.45>, 2006.
- 655 Crawford, I., Bower, K. N., Choulaton, T. W., Dearden, C., Crosier, J., Westbrook, C., Capes, G., Coe, H., Connolly, P. J., Dorsey, J. R., Gallagher, M. W., Williams, P., Trembath, J., Cui, Z., and Blyth, A.: Ice formation and development in aged, wintertime cumulus over the UK: observations and modelling, *Atmos. Chem. Phys.*, 12, 4963–4985, <https://doi.org/10.5194/acp-12-4963-2012>, 2012.
- Crosier, J., Bower, K., Choulaton, T., Westbrook, C. D., Connolly, P., Cui, Z., Crawford, I., Capes, G., Coe, H., Dorsey, J., et al.: Observations of ice multiplication in a weakly convective cell embedded in supercooled mid-level stratus, *Atmos. Chem. Phys.*, 11, 257–273, 2011.
- 660 Deshmukh, A., Phillips, V. T. J., Bansemmer, A., Patade, S., and Waman, D.: New Empirical Formulation for the Sublimational Breakup of Graupel and Dendritic Snow, *J. Atmos. Sci.*, 79, 317–336, <https://doi.org/https://doi.org/10.1175/JAS-D-20-0275.1>, 2022.
- Dong, Y. Y. and Hallett, J.: Droplet accretion during rime growth and the formation of secondary ice crystals, *Quart. J. Roy. Meteorol. Soc.*, 115, 127–142, 1989.
- 665 Dong, Y. Y., Oraltay, R. G., and Hallett, J.: Ice particle generation during evaporation, *Atmos. Res.*, 32, 45–53, [https://doi.org/10.1016/0169-8095\(94\)90050-7](https://doi.org/10.1016/0169-8095(94)90050-7), 1994.

- Duan, H., Romay, F., Li, C., Naqwi, A., Deng, W., and Liu, B.: Generation of Monodisperse Aerosols by Combining Aerodynamic Flow-Focusing and Mechanical Perturbation, *Aerosol Sci. Tech.*, 50, 17–25, <https://doi.org/10.1080/02786826.2015.1123213>, 2016.
- Dye, J. E. and Hobbs, P. V.: The influence on environmental parameters on freezing and fragmentation of suspended water drops, *J. Atmos. Sci.*, 25, 82–96, [https://doi.org/10.1175/1520-0469\(1968\)025<0082:tioepo>2.0.co;2](https://doi.org/10.1175/1520-0469(1968)025<0082:tioepo>2.0.co;2), 1968.
- Emersic, C. and Connolly, P.: Microscopic observations of riming on an ice surface using high speed video, *Atmos. Res.*, 185, 65–72, 2017.
- Erfani, E. and Mitchell, D. L.: Growth of ice particle mass and projected area during riming, *Atmos. Chem. Phys.*, 17, 1241–1257, 2017.
- Field, P. R., Lawson, R. P., Brown, P. R. A., Lloyd, G., Westbrook, C., Moisseev, D., Miltenberger, A., Nenes, A., Blyth, A., Choulaton, T., Connolly, P., Buehl, J., Crosier, J., Cui, Z., Dearden, C., DeMott, P., Flossmann, A., Heymsfield, A., Huang, Y., Kalesse, H., Kanji, Z. A., Korolev, A., Kirchgaessner, A., Lasher-Trapp, S., Leisner, T., McFarquhar, G., Phillips, V., Stüth, J., and Sullivan, S.: Secondary Ice Production: Current State of the Science and Recommendations for the Future, *Meteor. Mon.*, 58, 7.1 – 7.20, <https://doi.org/10.1175/AMSMONOGRAPHS-D-16-0014.1>, 2017.
- Georgakaki, P., Sotiropoulou, G., Vignon, E., Billault-Roux, A.-C., Berne, A., and Nenes, A.: Secondary ice production processes in winter-time alpine mixed-phase clouds, *Atmos. Chem. Phys.*, 22, 1965–1988, <https://doi.org/10.5194/acp-22-1965-2022>, 2022.
- Griggs, D. and Choulaton, T.: Freezing modes of riming droplets with application to ice splinter production, *Quart. J. Roy. Meteorol. Soc.*, 109, 243–253, 1983.
- Griggs, D. and Choulaton, T.: A laboratory study of secondary ice particle production by the fragmentation of rime and vapour-grown ice crystals, *Quart. J. Roy. Meteorol. Soc.*, 112, 149–163, 1986.
- Grzegorzczak, P., Yadav, S., Zanger, F., Theis, A., Mitra, S. K., Borrmann, S., and Szakáll, M.: Fragmentation of ice particles: laboratory experiments on graupel-graupel and graupel-snowflake collisions, *EGU sphere*, 2023, 1–31, <https://doi.org/10.5194/egusphere-2023-1074>, 2023.
- Hall, W. and Pruppacher, H.: The survival of ice particles falling from cirrus clouds in subsaturated air, *J. Atmos. Sci.*, 33, 1995–2006, 1976.
- Hallett, J. and Mossop, S.: Production of secondary ice particles during the riming process, *Nature*, 249, 26–28, 1974.
- Hare, D. and Sorensen, C.: The density of supercooled water. II. Bulk samples cooled to the homogeneous nucleation limit, *J. Chem. Phys.*, 87, 4840–4845, <https://doi.org/https://doi.org/10.1063/1.453710>, 1987.
- Harris-Hobbs, R. L. and Cooper, W. A.: Field evidence supporting quantitative predictions of secondary ice production-rates, *Journal of the Atmospheric Sciences*, 44, 1071–1082, [https://doi.org/10.1175/1520-0469\(1987\)044<1071:fesqpo>2.0.co;2](https://doi.org/10.1175/1520-0469(1987)044<1071:fesqpo>2.0.co;2), 1987.
- Heymsfield, A. and Willis, P.: Cloud Conditions Favoring Secondary Ice Particle Production in Tropical Maritime Convection, *J. Atmos. Sci.*, 71, 4500 – 4526, <https://doi.org/https://doi.org/10.1175/JAS-D-14-0093.1>, 2014.
- Heymsfield, A. J. and Mossop, S.: Temperature dependence of secondary ice crystal production during soft hail growth by riming, *Quart. J. Roy. Meteorol. Soc.*, 110, 765–770, 1984.
- Heymsfield, A. J. and Pflaum, J. C.: A quantitative assessment of the accuracy of techniques for calculating graupel growth, *J. Atmos. Sci.*, 42, 2264–2274, 1985.
- Hinds, W. C.: *Aerosol technology : properties, behavior, and measurement of airborne particles*, New York (N.Y.) : Wiley, 2nd ed. edn., <http://lib.ugent.be/catalog/rug01:000658373>, 1999.
- Hobbs, P. V.: Ice multiplication in clouds, *J. Atmos. Sci.*, 26, 315–318, 1969.
- Hobbs, P. V. and Rangno, A. L.: Ice particle concentrations in clouds, *J. Atmos. Sci.*, 42, 2523–2549, 1985.
- Hobbs, P. V. and Rangno, A. L.: Rapid development of high ice particle concentrations in small polar maritime cumuliform clouds, *J. Atmos. Sci.*, 47, 2710–2722, [https://doi.org/https://doi.org/10.1175/1520-0469\(1966\)023<0757:TEO AIS>2.0.CO;2](https://doi.org/https://doi.org/10.1175/1520-0469(1966)023<0757:TEO AIS>2.0.CO;2), 1990.

- 705 Hogan, R. J., Field, P., Illingworth, A., Cotton, R., and Choullarton, T.: Properties of embedded convection in warm-frontal mixed-phase cloud from aircraft and polarimetric radar, *Quart. J. Roy. Meteorol. Soc.*, 128, 451–476, 2002.
- Huang, Y., Chubb, T., Baumgardner, D., deHoog, M., Siems, S. T., and Manton, M. J.: Evidence for secondary ice production in Southern Ocean open cellular convection, *Quart. J. Roy. Meteorol. Soc.*, 143, 1685–1703, <https://doi.org/https://doi.org/10.1002/qj.3041>, 2017.
- James, R. L., Phillips, V. T., and Connolly, P. J.: Secondary ice production during the break-up of freezing water drops on impact with ice particles, *Atmos. Chem. Phys.*, 21, 18 519–18 530, 2021.
- 710 Jayaratne, E. and Grigos, D.: Electric charge separation during the fragmentation of rime in an airflow, *J. Atmos. Sci.*, 48, 2492–2495, 1991.
- Jensen, A. A. and Harrington, J. Y.: Modeling Ice Crystal Aspect Ratio Evolution during Riming: A Single-Particle Growth Model, *J. Atmos. Sci.*, 72, 2569–2590, <https://doi.org/https://doi.org/10.1175/JAS-D-14-0297.1>, 2015.
- Keinert, A., Spannagel, D., Leisner, T., and Kiselev, A.: Secondary ice production upon freezing of freely falling drizzle droplets, *J. Atmos. Sci.*, 77, 2959–2967, 2020.
- 715 King, W. D. and Fletcher, N. H.: Thermal Shock as an Ice Multiplication Mechanism. Part I. Theory, *J. Atmos. Sci.*, 33, 85 – 96, [https://doi.org/10.1175/1520-0469\(1976\)033<0085:TSAAIM>2.0.CO;2](https://doi.org/10.1175/1520-0469(1976)033<0085:TSAAIM>2.0.CO;2), 1976a.
- King, W. D. and Fletcher, N. H.: Thermal Shock as an Ice Multiplication Mechanism. Part II. Experimental, *J. Atmos. Sci.*, 33, 97–102, [https://doi.org/https://doi.org/10.1175/1520-0469\(1976\)033<0097:TSAAIM>2.0.CO;2](https://doi.org/https://doi.org/10.1175/1520-0469(1976)033<0097:TSAAIM>2.0.CO;2), 1976b.
- 720 Kleinheins, J., Kiselev, A., Keinert, A., Kind, M., and Leisner, T.: Thermal imaging of freezing drizzle droplets: pressure release events as a source of secondary ice particles, *J. Atmos. Sci.*, 78, 1703–1713, 2021.
- Koenig, L. R.: The Glaciating Behavior of Small Cumulonimbus Clouds, *J. Atmos. Sci.*, 20, 29 – 47, [https://doi.org/10.1175/1520-0469\(1963\)020<0029:TGBOSC>2.0.CO;2](https://doi.org/10.1175/1520-0469(1963)020<0029:TGBOSC>2.0.CO;2), 1963.
- Kolomeychuk, R. J., McKay, D. C., and Iribarne, J. V.: The Fragmentation and Electrification of Freezing Drops, *J. Atmos. Sci.*, 32, 974–979, [https://doi.org/10.1175/1520-0469\(1975\)032<0974:TFAEOF>2.0.CO;2](https://doi.org/10.1175/1520-0469(1975)032<0974:TFAEOF>2.0.CO;2), 1975.
- 725 Korolev, A. and Leisner, T.: Review of experimental studies of secondary ice production, *Atmos. Chem. Phys.*, 20, 11 767–11 797, <https://doi.org/10.5194/acp-20-11767-2020>, 2020.
- Korolev, A., Heckman, I., Wolde, M., Ackerman, A. S., Fridlind, A. M., Ladino, L. A., Lawson, R. P., Milbrandt, J., and Williams, E.: A new look at the environmental conditions favorable to secondary ice production, *Atmos. Chem. Phys.*, 20, 1391–1429, <https://doi.org/10.5194/acp-20-1391-2020>, 2020.
- 730 Kulkarni, P.: *Aerosol measurement: principles, techniques, and applications*, Wiley, Hoboken, NJ, 3. ed. edn., <http://onlinelibrary.wiley.com/book/10.1002/9781118001684>, includes bibliographical references and index. - Print version record, 2011.
- Ladino, L. A., Korolev, A., Heckman, I., Wolde, M., Fridlind, A. M., and Ackerman, A. S.: On the role of ice-nucleating aerosol in the formation of ice particles in tropical mesoscale convective systems, *Geophys. Res. Lett.*, 44, 1574–1582, 2017.
- 735 Lasher-Trapp, S., Leon, D. C., DeMott, P. J., Villanueva-Birriel, C. M., Johnson, A. V., Moser, D. H., Tully, C. S., and Wu, W.: A multisensor investigation of rime splintering in tropical maritime cumuli, *J. Atmos. Sci.*, 73, 2547–2564, 2016.
- Latham, J. and Mason, B. J.: Generation of electric charge associated with the formation of soft hail in thunderclouds, *Proc. R. Soc. Lond.*, 260, 537–549, <https://doi.org/https://doi.org/10.1098/rspa.1961.0052>, 1961.
- Lauber, A., Kiselev, A., Pander, T., Handmann, P., and Leisner, T.: Secondary ice formation during freezing of levitated droplets, *J. Atmos. Sci.*, 75, 2815–2826, 2018.
- 740 Lawson, R. P., Woods, S., and Morrison, H.: The microphysics of ice and precipitation development in tropical cumulus clouds, *J. Atmos. Sci.*, 72, 2429–2445, 2015.

- Li, H., Möhler, O., Petäjä, T., and Moisseev, D.: Two-year statistics of columnar-ice production in stratiform clouds over Hyytiälä, Finland: environmental conditions and the relevance to secondary ice production, *Atmos. Chem. Phys.*, 21, 14 671–14 686, 2021.
- 745 Libbrecht, K. G.: Physical dynamics of ice crystal growth, *Annu. Rev. Mater. Res.*, 47, 271–295, 2017.
- Ludlam, F. H.: *The hail problem*, Unione nazionale antigrandine, 1958.
- Luke, E. P., Yang, F., Kollias, P., Vogelmann, A. M., and Maahn, M.: New insights into ice multiplication using remote-sensing observations of slightly supercooled mixed-phase clouds in the Arctic, *P. Natl. Acad. Sci.*, 118, e2021387 118, 2021.
- Macklin, W.: The density and structure of ice formed by accretion, Tech. rep., Imperial Coll. of Science and Technology London (England),
750 1960.
- Macklin, W.: The density and structure of ice formed by accretion, *Quart. J. Roy. Meteorol. Soc.*, 88, 30–50, 1962.
- Macklin, W. and Payne, G.: A theoretical study of the ice accretion process, *Quart. J. Roy. Meteorol. Soc.*, 93, 195–213, 1967.
- Macklin, W. and Payne, G.: Some aspects of the accretion process, *Quart. J. Roy. Meteorol. Soc.*, 94, 167–175, 1968.
- Macklin, W. and Payne, G.: The spreading of accreted droplets, *Quart. J. Roy. Meteorol. Soc.*, 95, 724–730, 1969.
- 755 Mason, B. J. and Maybank, J.: The fragmentation and electrification of freezing water drops, *Quart. J. Roy. Meteor. Soc.*, 86, 176–185, <https://doi.org/10.1002/qj.49708636806>, 1960.
- Mossop, S.: Production of secondary ice particles during the growth of graupel by riming, *Quart. J. Roy. Meteorol. Soc.*, 102, 45–57, 1976.
- Mossop, S.: The influence of drop size distribution on the production of secondary ice particles during graupel growth, *Quart. J. Roy. Meteorol. Soc.*, 104, 323–330, 1978a.
- 760 Mossop, S.: Secondary ice particle production during rime growth: The effect of drop size distribution and rimer velocity, *Quart. J. Roy. Meteorol. Soc.*, 111, 1113–1124, 1985a.
- Mossop, S. and Hallett, J.: Ice crystal concentration in cumulus clouds: Influence of the drop spectrum, *Science*, 186, 632–634, 1974.
- Mossop, S., Brownscombe, J., and Collins, G.: The production of secondary ice particles during riming, *Quart. J. Roy. Meteorol. Soc.*, 100, 427–436, 1974.
- 765 Mossop, S. C.: Some factors governing ice particle multiplication in cumulus clouds, *Journal of the Atmospheric Sciences*, 35, 2033–2037, [https://doi.org/10.1175/1520-0469\(1978\)035<2033:sfgipm>2.0.co;2](https://doi.org/10.1175/1520-0469(1978)035<2033:sfgipm>2.0.co;2), 1978b.
- Mossop, S. C.: The Origin and Concentration of Ice Crystals in Clouds, *Bull. Amer. Meteorol. Soc.*, 66, 264–273, [https://doi.org/10.1175/1520-0477\(1985\)066<0264:TOACOI>2.0.CO;2](https://doi.org/10.1175/1520-0477(1985)066<0264:TOACOI>2.0.CO;2), 1985b.
- Murphy, D. M. and Koop, T.: Review of the vapour pressures of ice and supercooled water for atmospheric applications, *Quart. J. Roy. Meteorol. Soc.*, 131, 1539–1565, <https://doi.org/https://doi.org/10.1256/qj.04.94>, 2005.
- 770 Oraltay, R. G. and Hallett, J.: Evaporation and Melting of Ice Crystals: A Laboratory Study, *Atmos. Res.*, 24, 169–189, [https://doi.org/10.1016/0169-8095\(89\)90044-6](https://doi.org/10.1016/0169-8095(89)90044-6), 1989.
- O’Shea, S. J., Choulaton, T. W., Flynn, M., Bower, K. N., Gallagher, M., Crosier, J., Williams, P., Crawford, I., Fleming, Z. L., Listowski, C., Kirchgaessner, A., Ladkin, R. S., and Lachlan-Cope, T.: In situ measurements of cloud microphysics and aerosol over coastal Antarctica during the MAC campaign, *Atmos. Chem. Phys.*, 17, 13 049–13 070, <https://doi.org/10.5194/acp-17-13049-2017>, 2017.
- 775 Phillips, V. T. J., Patade, S., Gutierrez, J., and Bansemer, A.: Secondary Ice Production by Fragmentation of Freezing Drops: Formulation and Theory, *J. Atmos. Sci.*, 75, 3031 – 3070, <https://doi.org/https://doi.org/10.1175/JAS-D-17-0190.1>, 2018.
- Prabhakaran, P., Kinney, G., Cantrell, W., Shaw, R. A., and Bodenschatz, E.: High supersaturation in the wake of falling hydrometeors: Implications for cloud invigoration and ice nucleation, *Geophys. Res. Lett.*, 47, e2020GL088 055, 2020.

- 780 Pruppacher, H. and Klett, J.: *Microphysics of Clouds and Precipitation*, vol. 18, Springer Dordrecht Heidelberg London New York, <https://doi.org/10.1007/978-0-306-48100-0>, 2010.
- Ramelli, F., Henneberger, J., David, R. O., Bühl, J., Radenz, M., Seifert, P., Wieder, J., Lauber, A., Pasquier, J. T., Engelmann, R., et al.: Microphysical investigation of the seeder and feeder region of an Alpine mixed-phase cloud, *Atmos. Chem. Phys.*, 21, 6681–6706, 2021.
- Saunders, C. and Hosseini, A.: A laboratory study of the effect of velocity on Hallett–Mossop ice crystal multiplication, *Atmos. Res.*, 59, 785 3–14, 2001.
- Schumann, T.: The theory of hailstone formation, *Quart. J. Roy. Meteorol. Soc.*, 64, 3–21, 1938.
- Sotiropoulou, G., Sullivan, S., Savre, J., Lloyd, G., Lachlan-Cope, T., Ekman, A. M., and Nenes, A.: The impact of secondary ice production on Arctic stratocumulus, *Atmos. Chem. Phys.*, 20, 1301–1316, 2020.
- Sullivan, S. C., Hoose, C., Kiselev, A., Leisner, T., and Nenes, A.: Initiation of secondary ice production in clouds, *Atmos. Chem. Phys.*, 18, 790 1593–1610, 2018.
- Sun, J., Ariya, P. A., Leighton, H. G., and Yau, M.: Mystery of ice multiplication in warm-based precipitating shallow cumulus clouds, *Geophys. Res. Lett.*, 37, 2010.
- Takahashi, C. and Yamashita, A.: Production of Ice Splinters by the Freezing of Water Drops in Free Fall, *J Meteorol. Soc. Jpn.*, 55, 139–141, https://doi.org/10.2151/jmsj1965.55.1_139, 1977.
- 795 Takahashi, T., Nagao, Y., and Kushiyama, Y.: Possible high ice particle production during Graupel-Graupel collisions, *J. Atmos. Sci.*, 52, 4523–4527, [https://doi.org/10.1175/1520-0469\(1995\)052<4523:phippd>2.0.co;2](https://doi.org/10.1175/1520-0469(1995)052<4523:phippd>2.0.co;2), 1995.
- Taylor, J., Choulaton, T., Blyth, A., Liu, Z., Bower, K., Crosier, J., Gallagher, M., Williams, P. I., Dorsey, J., Flynn, M., et al.: Observations of cloud microphysics and ice formation during COPE, *Atmos. Chem. Phys.*, 16, 799–826, 2016.
- Vardiman, L.: Generation of secondary ice particles in clouds by crystal-crystal collision, *J. Atmos. Sci.*, 35, 2168–2180, 800 [https://doi.org/10.1175/1520-0469\(1978\)035<2168:tgosip>2.0.co;2](https://doi.org/10.1175/1520-0469(1978)035<2168:tgosip>2.0.co;2), 1978.
- Wang, P. K.: *Collision, coalescence, breakup, and melting*, p. 252–287, Cambridge University Press, <https://doi.org/10.1017/CBO9780511794285.011>, 2013.
- Wildeman, S., Sterl, S., Sun, C., and Lohse, D.: Fast Dynamics of Water Droplets Freezing from the Outside In, *Phys. Rev. Lett.*, 118, 084 101, <https://doi.org/10.1103/PhysRevLett.118.084101>, 2017.
- 805 Yano, J.-I., Phillips, V. T., and Kanawade, V.: Explosive ice multiplication by mechanical break-up in ice–ice collisions: a dynamical system-based study, *Quart. J. Roy. Meteorol. Soc.*, 142, 867–879, 2016.
- Zhao, X. and Liu, X.: Global Importance of Secondary Ice Production, *Geophys. Res. Lett.*, 48, e2021GL092581, <https://doi.org/https://doi.org/10.1029/2021GL092581>, e2021GL092581 2021GL092581, 2021.
- Zhao, X., Liu, X., Burrows, S., DeMott, P. J., Diao, M., McFarquhar, G. M., Patade, S., Phillips, V., Roberts, G. C., Sanchez, 810 K. J., Shi, Y., and Zhang, M.: Important Ice Processes Are Missed by the Community Earth System Model in Southern Ocean Mixed-Phase Clouds: Bridging SOCRATES Observations to Model Developments, *Geophys. Res. Atmos.*, 128, e2022JD037513, <https://doi.org/https://doi.org/10.1029/2022JD037513>, 2023.